# Digital Twins for Rapid In-situ Qualification of Part Quality in Laser Powder Bed Fusion Additive Manufacturing

Benjamin D. Bevans<sup>1</sup>, Antonio Carrington<sup>1</sup>, Alex Riensche<sup>1</sup>, Adriane Tenequer<sup>2</sup>, Christopher Barrett<sup>3</sup>, Harold (Scott) Halliday<sup>2</sup>, Raghavan Srinivasan<sup>4</sup>, Kevin D. Cole<sup>5</sup>, Prahalada Rao<sup>1,6</sup>

#### **Abstract**

This work concerns the laser powder bed fusion (LPBF) additive manufacturing process. Currently, LPBF parts are inspected post-process using such techniques as X-ray computed tomography, optical and scanning electron microscopy, among others. This empirical build-and-test approach for qualification of part quality is prohibitively expensive and cumbersome. To enable rapid and accurate in-situ qualification of LPBF part quality, in this work, we developed a physics and data-integrated *digital twin* approach. To demonstrate the approach, Inconel 718 parts of various shapes were manufactured under differing LPBF processing conditions. The process was continuously monitored using in-situ thermal and optical tomography imaging cameras. The part-scale thermal history was predicted using an experimentally validated computational thermal simulation. The simulation-derived thermal history and sensor signatures were used as inputs to a k-nearest neighbor machine learning model. The machine learning model was trained with ground truth porosity and microstructure data obtained from post-process characterization. The approach predicted the onset of porosity, meltpool depth, grain size, and microhardness with an accuracy exceeding 90% (R²). This work thus takes a critical step towards realizing an in-situ *Born Qualified* part quality assessment paradigm in LPBF.

**Keywords:** Laser powder bed fusion, digital twin, thermal and optical imaging, thermal simulations, porosity, microstructure prediction, Inconel 718.

<sup>&</sup>lt;sup>1</sup>Industrial and Systems Engineering, Virginia Polytechnical Institute, Blacksburg, VA, USA

<sup>&</sup>lt;sup>2</sup>Center for Advanced Manufacturing, Navajo Technical University, Crownpoint, NM, USA

<sup>&</sup>lt;sup>3</sup>Laser Fusion Solutions, LLC, Fairborn OH, USA

<sup>&</sup>lt;sup>4</sup>Mechanical and Materials Engineering, Wright State University, Dayton, OH, USA

<sup>&</sup>lt;sup>5</sup> Mechanical and Materials Engineering, University of Nebraska-Lincoln, Lincoln, NE

<sup>&</sup>lt;sup>6</sup>Mechanical Engineering, Virginia Polytechnical Institute, Blacksburg, VA, USA

#### 1 Introduction

# 1.1 Objective and Motivation

The objective of this work is to predict porosity and microstructure-related characteristics of Inconel 718 parts made using the laser powder bed fusion (LPBF) additive manufacturing (AM) process. To realize this objective, we developed and applied a physics and data-integrated *digital twin* approach. The key idea is to use part-level thermal history estimated from a physics-based process simulation and real-time data acquired from an heterogenous in-situ sensor array as inputs to a machine learning model. The machine learning model is trained to predict lack-of-fusion porosity, and three microstructure-related characteristics, namely, solidified meltpool depth, grain size and microhardness. The foregoing porosity and microstructure characteristics are consequential to functional properties, such as strength and fatigue life [1-3].

In the LPBF process, as visualized in Figure 1, a thin layer (~30 µm) of metal powder is spread on a substrate and selectively fused with energy from a scanning laser [4, 5]. This process is favored for its ability to manufacture intricate, high-performance and high-value components; reduce weight and part count in assemblies; and enhance responsiveness and resiliency of the manufacturing supply chain [6, 7].

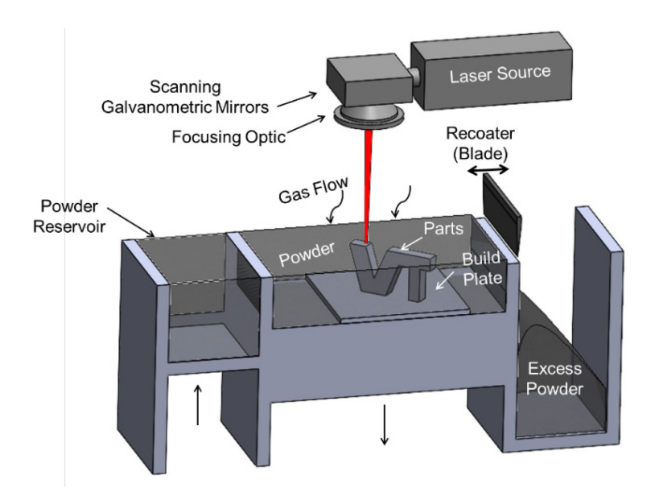


Figure 1: A schematic of the laser powder bed fusion (LPBF) additive manufacturing process.

Despite these compelling advantages, safety-critical aerospace and defense sectors have been slow to adopt LPBF due to the tendency of the process to form flaws, which causes large part-to-part variation in functional properties [8-11]. As exemplified in the context of Figure 2, these deleterious flaws range across multiple scales from inconsistencies in the microstructure and porosity at the microscale, to macro-scale cracking and deformation. Consequently, to ensure the quality of LPBF parts, an extensive empirical build-and-test approach is often mandated [12]. Parts are manufactured under *a priori* optimized processing conditions, followed by post-process non-destructive and destructive characterization. It is estimated that such empirical-driven frameworks for part qualification cost millions of dollars and require multiple years' effort [13-16].

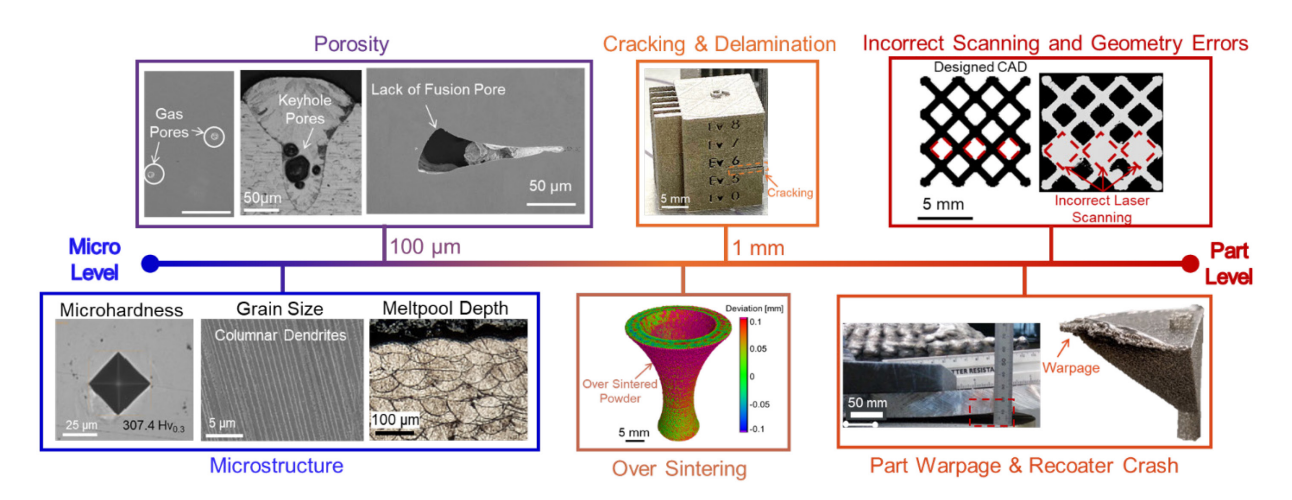


Figure 2: The multi-scale nature of flaw formation in LPBF. This work focuses on detection of lack-of-fusion porosity, microhardness, grain size, and meltpool depth.

One common approach for non-destructive inspection of porosity, surface texture, and geometric integrity of internal surfaces is X-ray computed tomography (X-ray CT). The fidelity of X-ray CT is contingent on the material and geometry of the sample [17]. The interaction of X-rays with the part geometry, along with motion-, temperature-, humidity- and reconstruction-related noise effects can cause artefacts, such as beam hardening, streaking, and distortion, among others [17]. For examination of dense alloys, e.g., Inconel and Stainless Steel, the X-ray beam is

progressively attenuated with increasing thickness of the sample [18]. With a typical 225 kV X-ray source the maximum thickness of Stainless Steel that can be penetrated is ~25 mm [19, 20]. Hence, despite recent advances in precision beam positioning and image reconstruction, it often requires several hours to X-ray CT parts made from dense alloys [18]. The restricted penetration of X-ray CT for dense materials entails that only larger flaws, typically greater than 50 μm, can be detected reliably. Further, the limited resolution of X-ray CT is insufficient to characterize microstructural aspects, such as meltpool depth and grain size [17].

To quantify microstructural characteristics, representative coupons are manufactured alongside the actual component [14]. These so-called witness coupons, which are typically simple cuboid or cylindrical geometries, are characterized using metallographic techniques, such as optical and scanning electron microscopy, among others [3, 21]. This witness coupon approach for indirect qualification of the microstructure is prone to uncertainty [14]. This is because, different LPBF part shapes, albeit produced under identical processing parameters, seldom result in similar microstructure, owing to variations in their thermal history and inherent process stochasticity [22].

To explain further, it is implicitly assumed that the witness coupon would have microstructure characteristics similar to the actual part. However, the spatiotemporal temperature distribution of a part, also called the thermal history, is a key determinant of flaw formation and microstructure evolved [23]. Apart from processing parameters and part shape, the thermal history is influenced by several factors [24]. Researchers have reported that minor changes in the part orientation, build layout, including addition and removal of other parts from a build plate, adding pauses between layers, among others, can substantially alter the thermal history resulting in differences in microstructure evolved [25-27]. Consequently, the assumed similitude of the microstructure evolved between a standardized witness coupon and actual part is suspect.

# 1.2 Hypothesis, Approach and Limitations

The hypothesis of this work is that a digital twin strategy combining real-time information from heterogeneous in-situ sensors and thermal history estimated with a physics-based model would predict porosity and microstructure-related characteristics in LPBF parts with greater statistical accuracy than either sensor data-driven modeling or physics-based modeling alone.

The approach to test this hypothesis is outlined in Figure 3. We manufactured Inconel 718 parts encompassing 22 different shapes and LPBF process parameter combinations. During the process, optical tomography and thermal imaging data were acquired from an in-situ sensor suite. Features (process signatures) were extracted from the sensor data. The thermal history of each part was predicted using an experimentally validated physics-based computational model. The process signatures and model-derived thermal history aspects were subsequently combined in a computationally tractable machine learning model (k-nearest neighbors, kNN). The kNN machine learning model was trained on offline metallographic characterization data to predict porosity, meltpool depth, grain size, and microhardness.

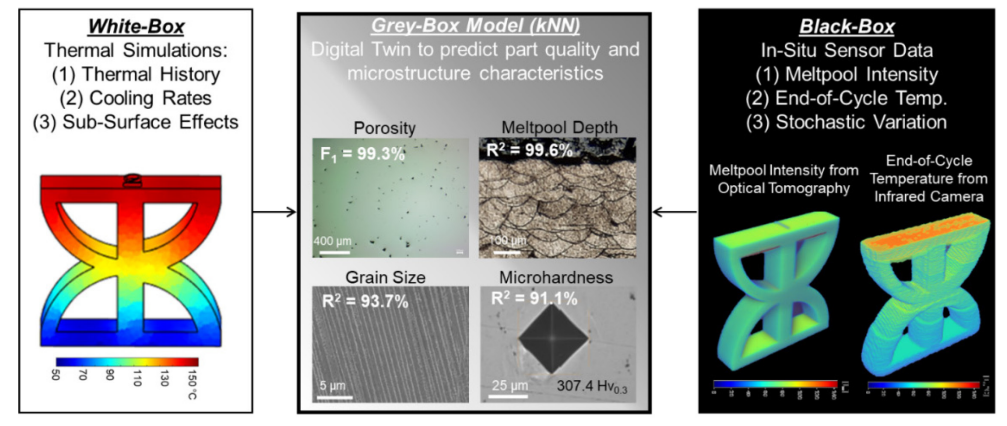


Figure 3: The digital twin approach implemented in this work. Physics-based model predictions of the part-scale thermal history are combined with in-situ process signatures inside machine learning.

There are two limitations in this work. First, it does not consider detailed microstructure aspects, such as grain texture and orientation, material composition and segregation, and material

phases that occur in LPBF of Inconel 718 [3]. Nor does it predict the effect of microstructure on mechanical properties. Characterizing the foregoing microstructure aspects requires techniques such as electron back scatter diffraction and X-ray diffraction. These measurements are cumbersome and expensive to acquire for an entire part due to their localized nature [28].

Second, in LPBF, physical models are stratified into three phenomenological scales, namely, (i) micro-scale, meltpool-level thermal-fluid phenomena (< 100 μm); (ii) meso-scale, track- and layer-level solidification (100 to 500 μm); and (iii) macro-scale, part-level thermal gradients (> 500 μm) [29]. In this work, macro-scale, part-level thermal history is predicted, and the track-level and meltpool-level thermal-fluid phenomena are not considered. In the literature, the track- and meltpool-level thermal-fluid phenomena are modeled as a Navier-Stokes system [30, 31]. The part-level thermal phenomena are predicted by solving the heat diffusion equation, a linear differential equation which is more computationally tractable [32-34]. Consolidating multi-scale phenomena is avoided due to its prohibitive computational burden [29]. This drawback is addressed by incorporating in-situ sensor data that partially captures meltpool-level phenomena.

The rest of this paper is organized as follows. Sec. 2 provides an overview of the literature with respect to porosity and microstructure prediction in LPBF along with a summary of the state-of-the-art relating to the implementation of digital twins in additive manufacturing. Sec. 3 details the experimental setup, design of experiments, and post-process measurement of part quality. The digital twin methodology is detailed in Sec. 4 in the context of the acquired sensor signatures, calibration and validation of the graph theory-based thermal model, and the machine learning model. The results are reported in Sec. 5, stratified into prediction of porosity, meltpool depth, grain size, and microhardness. Conclusions and future work are summarized in Sec. 6.

# 2 Prior Work and Challenges

## 2.1 Sensor-based Monitoring and Machine Learning

As an alternative to *post-process* empirical assessment, researchers have explored using insitu sensor data for qualification of LPBF parts [35]. As evident from recent review articles, insitu sensor data, such as infrared thermal imaging, pyrometry, optical imaging, among others, have been used extensively to detect porosity, and macro-scale part warpage and recoater crashes [36-38]. The sensor data is correlated to specific flaws using data-driven, machine learning models e.g., Gaussian process modeling, neural networks, deep learning, among others [39-43].

There is a large body of prior research demonstrating detection of lack-of-fusion porosity using in-situ sensor data [44, 45]. For example, Smoqi *et. al.* [46] used a two-wavelength imaging pyrometer for the detection of lack-of-fusion and keyhole porosity in LPBF. From meltpool images acquired from a two-wavelength imaging pyrometer, Smoqi *et. al.* [46] extracted signatures, such as meltpool shape and temperature distribution, and used these as inputs to machine learning models. These models were trained to classify the type of porosity (keyhole and lack-of-fusion porosity) and its severity with fidelity exceeding 97% F<sub>1</sub>-score. Likewise, Nguyen *et. al.* [47] instrumented an optical camera into an LPBF machine to monitor the top surface of the powder bed. These images were subsequently used as inputs into deep neural networks trained to predict lack-of-fusion porosity with statistical fidelity over 95%.

Predicting meltpool depth has remained relatively unstudied in LPBF in comparison to other material characteristics. The meltpool depth (d<sub>p</sub>), which has been recently suggested by NASA as an indicator of process stability, refers to the depth of the solidified meltpool at the topmost layer relative to the layer height set on the machine [48]. *In a recent work, Mossallanejad et. al.* [49] used processing parameters along with known material properties of various popular alloys to

predict the meltpool depth with a statistical accuracy  $\sim 90\%$  ( $R^2$ ). Several results correlating microhardness to the processing conditions have been presented in the literature [50, 51]. Recently, Zhang et. al. [52] used data from a photodiode instrumented coaxial to the laser with a random forest machine learning model to predict microhardness with an accuracy exceeding 90% ( $R^2$ ). However, these models do not account for the effect of the thermal history.

Prediction of microstructural characteristics, such as grain size, using sensor data is in its infancy [53]. This is because microstructure evolution is contingent on both surface-level phenomena, as well as sub-surface temperature and cooling rates [54]. In LPBF, because the part is progressively buried under powder, existing sensing approaches, such as infrared and optical imaging, cannot penetrate the top surface of the part. Consequently, existing sensing approaches are incapable of observing the sub-surface thermal phenomena that influence microstructure evolution. Albeit, ultrasound and laser acoustic spectroscopy approaches have been implemented for ex-situ, non-destructive microstructure characterization [55-57].

Despite the success of these prior works, there are two main drawbacks in using purely datadriven machine learning for assessment of part quality.

• Typically, data-driven models, are trained based on sensor data obtained for simple cuboid or cylinder-shaped coupons [58]. These models are adept at detecting one type of flaw, such as porosity, often based on data from one type of sensor [44, 59]. However, such data-driven approaches perform poorly when applied to practical, complex shapes [60]. In other words, the scalability and transferability of purely data-driven approaches is poor, because they ignore the causal effect of part shape and material properties on the thermal phenomena that cause flaw formation [42].

• Machine learning models, due to their black-box nature, occlude interpretability and are reactive in nature, which mitigates their ability to prevent and correct flaw formation [61, 62]. Further, machine learning models rely on extensive datasets, and the sensor data (input) and flaws (outputs) must be aligned spatially. These data sets are expensive to obtain given the small batch sizes of LPBF, and the expense associated with obtaining ground truth characterization data [63].

# 2.2 Physics-based Modeling

Three physics-based approaches are currently popular for the prediction of microstructural characteristics in LPBF, these are: (i) cellular automaton, (ii) Monte Carlo, and (iii) phase-field modeling [64, 65]. Using these methods, an image-based representation of the predicted microstructure can be generated [23, 66]. Researchers have successfully used these microstructure evolution models to predict the grain shape, orientation, and texture [61, 67, 68].

However, these physics-based models are computationally demanding. They require several days to predict the evolved microstructure for only a few layers [30, 69, 70]. Consequently, prediction of microstructural characteristics using physics-based models have been used primarily for small, local regions in place of simulating the entire part geometry [71]. Another drawback with using physics-based models for part qualification is that they do not consider the inherent stochasticity of the LPBF process.

# 2.3 Combined Physics and Data-driven Modeling (Digital Twin)

An emerging approach to enable rapid qualification of LPBF parts is called grey-box modeling, which combines predictions from physics-based (white-box) models and real-time sensor data with the predictive ability of machine learning (black-box modeling) [54, 72]. Another name for the approach is the digital twin, owing to its integration of an *a priori* model of the

process with real-time data concerning its current state. The rationale for the grey-box or digital twin approach is that it augments the interpretability of physics-based models with real-time information of the process state from sensor data [73]. Thus, both the causal physical phenomena and stochastic aspects inherent to the process are combined.

Recent review articles concerning data- and physics-integrated modeling of AM are provided by Kouraytem *et. al.* [74], Shen *et. al.* [75], Gunasegaram *et. al.* [76], Mukherjee *et. al.* [54], Zhang *et. al.* [77], and Guo *et. al.* [78]. These review articles delineate the need and utility of the digital twin for AM in the following contexts: (1) in-situ monitoring, prediction, and control of process state including flaw formation and microstructure; (2) mitigate the computational burden of the multi-scale physics-based models; (3) overcome the lack of interpretability and bias inherent to machine learning models; (4) accelerate parameter optimization and process qualification across different materials and systems from sparse data; and (5) obtain site specific microstructure, i.e., functional grading of the microstructure.

Gunasegaram *et. al.* [76] note that a key constraint limiting the implementation of digital twins in AM is in the computational burden and proprietary nature of commercial packages currently available for physics-based modeling. They also underscore the importance of cross-validation between black- and white-box modeling inside of the digital-twin, in which the output of the physics-based model is compared to the real-world sensor data. We overcome the foregoing drawbacks, noted by Gunasegaram *et. al.* [76], by employing an experimentally validated, computationally tractable thermal simulation model [24, 27]. We also provide a visual, as well as statistical correlation between the physics-based model and sensor data for lack-of-fusion porosity and each type of microstructure characteristic predicted.

Feng *et. al.* [79] classified the potential uses for digital twins in AM into three levels. Level 3 is in-situ monitoring of process drifts and flaw formation; Level 2 the prediction of microstructural characteristics, and Level 1 the prediction of mechanical properties. This work straddles Levels 3 and 2 of Feng *et. al.* 's [79] hierarchical classification of digital twins. Our future works will attempt to encompass all three levels.

As an example of a Level 3-type of application of digital twin for process monitoring, Roy *et. al.* [80] continually tracked the status of a friction stir deposition AM machine using sensors, such as oil level, rotary sensors, turbidity sensor, and other machine-level sensors. These sensors tracked variations in the machine status from the predetermined target level. By monitoring the variation between the ideal condition and actual states, appropriate maintenance actions were successfully recommended using a simple support vector machine learning model.

A recent work by Riensche *et. al.* [81] demonstrates a Level 2-type use case of the digital twin toward predicting the microstructure. Aspects of the thermal history, such as cooling time and end-of-cycle temperature were estimated from a part-level thermal simulation. These simulation-derived features were subsequently used as inputs to a simple support vector machine learning model trained to classify the meltpool penetration depth and grain size with accuracy exceeding 80% (statistical F<sub>1</sub>-score). However, no in-situ data was used to supplement model predictions. The current paper augments the work of Riensche *et. al.* [81] by combining physics-derived thermal history aspects with statistical features (signatures) extracted from in-situ sensor data for the prediction of lack-of-fusion porosity, meltpool depth, grain size, and microhardness.

# 3 Experiments

#### 3.1 Setup

As shown in Figure 4, an optical tomography and longwave infrared thermal camera were installed on an Open Additive Panda LPBF machine. The sensor specifications and resolutions are provided in Table 1. These sensors are synchronized in time and capture complementary process phenomena. The optical tomography camera tracks the thermal behavior at the local, meltpool-scale initiated by the rapid transition of the laser. The thermal camera acquires the global, layerwise surface temperature. Representative sensor data obtained in this work are shown in Figure 5.

The optical tomography camera was installed on top of the machine at an 83° angle to the horizontal. The camera is equipped with a near infrared bandpass filter (~800 nm) and is set for an exposure time of 250 ms with a pixel resolution of 346 pixels per mm² as detailed in Table 1. This relatively long exposure time allows tracking the most intense light radiated for every image pixel scanned by the laser. In other words, the optical tomography camera tracks the nearly instantaneous heating (106 °C·s<sup>-1</sup>) initiated by the laser strike and captures the relative meltpool intensity of every pixel for every layer [82, 83].

A Micro-Epsilon TIM 640 infrared thermal camera was installed inside the build chamber at a 60° angle to the horizontal. It captures thermal images of the powder bed at a rate of 30 Hz continuously for the entire duration of the build with a pixel resolution of 10 pixels per mm² as detailed in Table 1. The thermal camera measures the longwave infrared (LWIR) radiation in the range of 8 μm to 14 μm. Such LWIR thermal cameras have been typically used in LPBF for tracking the temperature of the top surface of the powder bed after the laser has melted a layer, and a new layer is deposited on top but is yet to be melted [25, 84]. This signature, termed the end-of-cycle temperature (T<sub>e</sub>), or inter-layer temperature, and described later in Sec. 4.1.1, has been

linked to part-scale thermal phenomena and microstructure evolution [27, 81]. In this work, the relative temperature readings of the LWIR thermal camera were calibrated to absolute scale using an industry standard procedure that references in-process thermocouple measurements [24].

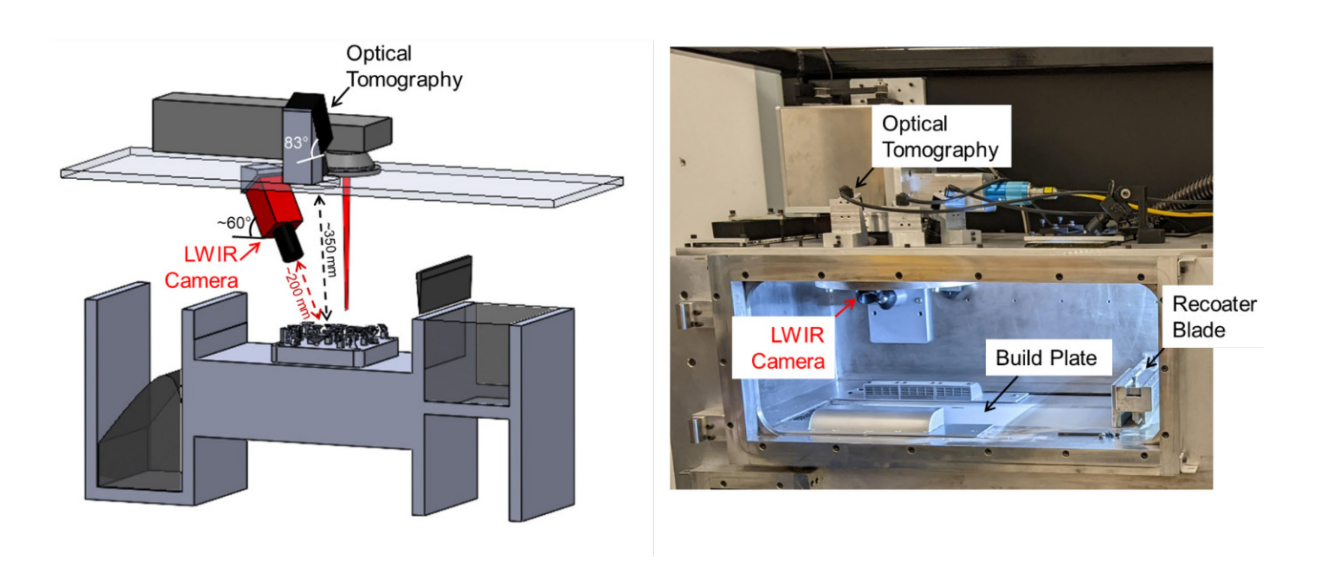


Figure 4: Location and positioning of the optical tomography and infrared thermal camera in the LPBF machine.

# 3.2 Design of Experiments

#### 3.2.1 Exemplar Parts

As shown in Figure 5, 22 Inconel 718 parts of different shapes were manufactured under varying processing conditions. The build consisted of 733 layers and required ~6 hours to finish. Inconel 718 is a precipitation hardening nickel-based alloy that is favored in high-temperature applications [3, 28]. Of the 22 parts on the build plate, herein we study 18 parts encompassing six different shapes. Representative thermal and optical imaging data for three layers obtained during the build are depicted in Figure 5(c) and (d), respectively.

As detailed in Figure 6, the shapes studied in this work are labeled as follows: psi (Ψ), solid vase (VS), hollow vase (VH), cone (C), overhang (O), and tower (T). All parts are 22 mm tall (733 layers), except for the cone, viz., 15 mm tall (500 layers). None of the parts had visually apparent

flaw formation, such as warpage or delamination, and the build was never halted to rectify any errors. These part geometries (Figure 6) have features, such as steep overhangs, thin walls, and enclosed cavities that would engender complex thermal history trends, and consequently, induce variation in the microstructure [85]. Similar part shapes have been studied in our previous work [26, 27, 81]. The rationale for each type of part shape is described herewith in the context of Figure 6, and their processing conditions are described in the following Sec. 3.2.2

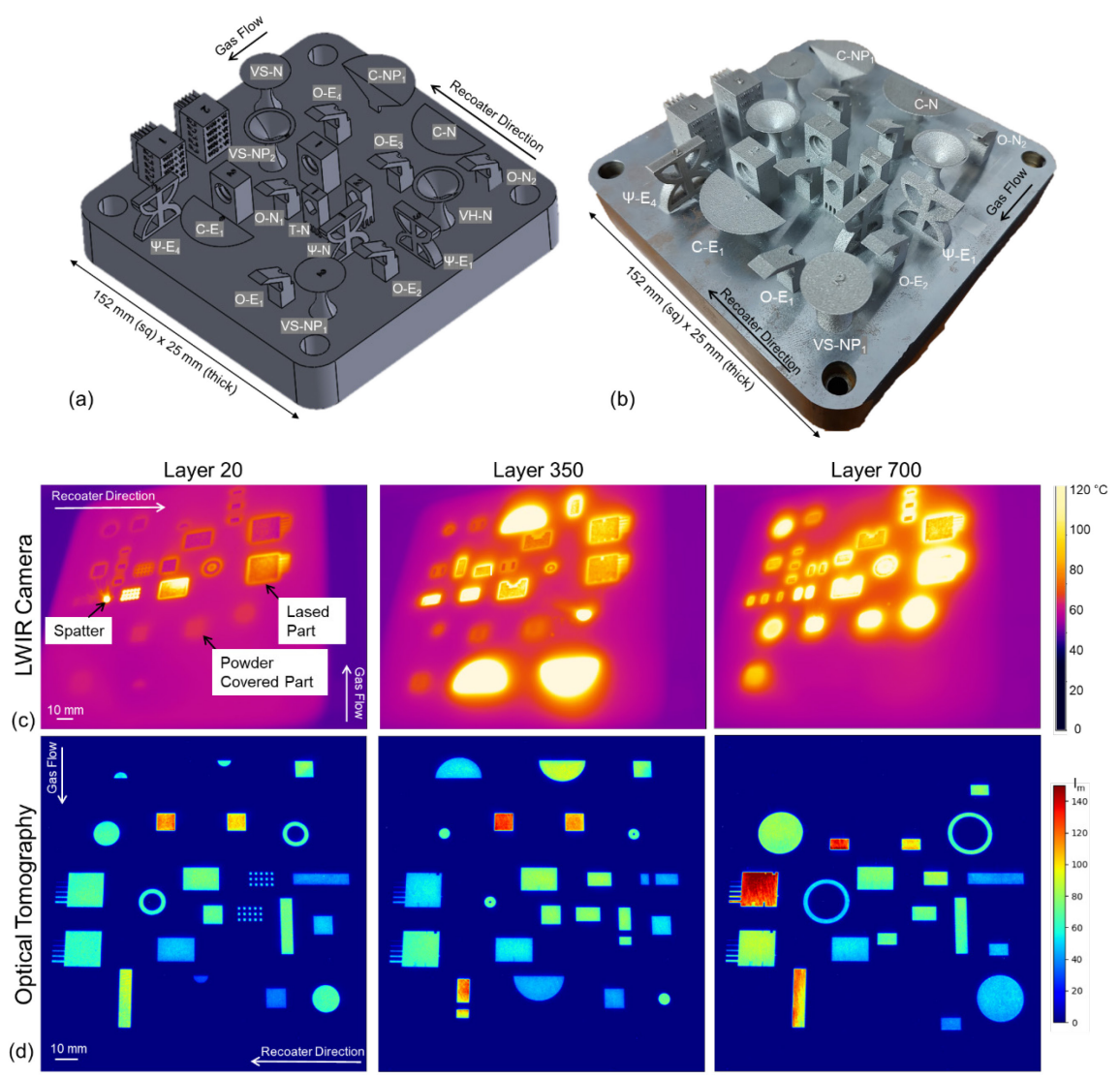


Figure 5: (a) CAD diagram and (b) physical picture of the build plate used in this work. Note that there are no visually apparent flaw formation such as warpage or delamination. Three layers of representative data from the (c) longwave infrared (LWIR) thermal camera and (d) optical tomography camera.

# (a) Psi (Ψ)

Three psi-shaped (Ψ) geometries were manufactured under different processing conditions. Each psi-shaped part has a central pillar flanked by two arches with differing wall thickness to facilitate differential heat dissipation.

# (b) Vase (VS & VH)

A total of four vase-shaped parts were manufactured under varying processing conditions. Two of these vases were hollow (VH) and had a 1 mm central cavity, and two solid vases (VS) did not have a central cavity.

# (c) Cone (C)

Three cone geometries (C) with a 35° overhang angle were manufactured. In our prior works, it was observed that the latter layers of the cone-shaped geometries tend to retain heat, resulting in grain coarsening [26, 27].

# (d) Overhang (O)

The six overhang geometries (O) with 30° angle from the horizontal were manufactured under different processing conditions. These geometries contain an 8×8×10 mm cuboid section at the bottom and two struts supporting the overhang section. In our previous works, we observed that the overhang section tends to retain heat contingent on the processing conditions resulting in different microstructure evolution [26].

#### (e) Tower (T)

Two tower geometries (T) were manufactured under different processing conditions. The powder trapped in the hexagonal cavity and thin-wall struts at the bottom tend to impede heat flux through the part, resulting in heat retention.

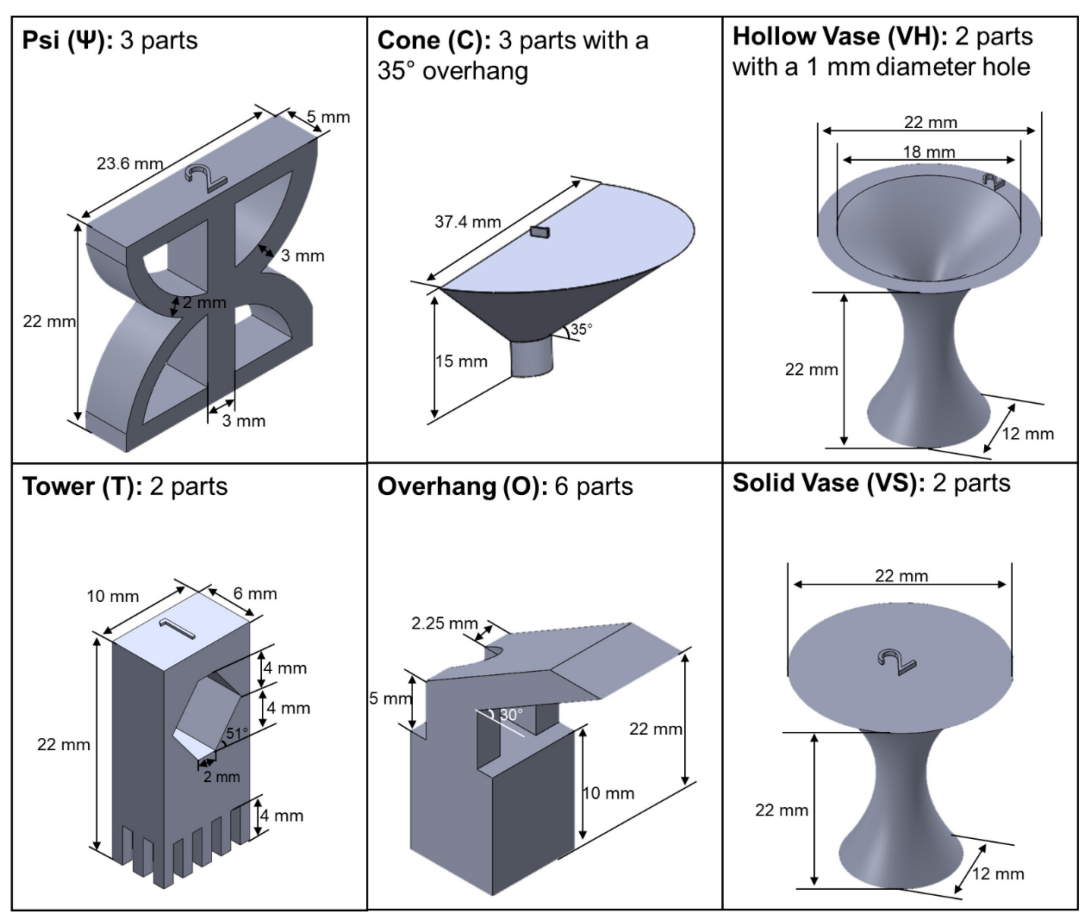


Figure 6: Schematic of the 6 types of part shapes (geometries) studied in this work.

# 3.2.2 Processing conditions

As depicted in Figure 7, the parts were built under varying laser power (P) and scan velocity (V) conditions. The treatment conditions labeled P<sub>1</sub>-P<sub>4</sub> represent changes in laser power (P) only, and those labeled E<sub>1</sub>-E<sub>4</sub> incorporate changes in both P and V simultaneously. The processing parameter combinations span a wide range of energy densities (E<sub>v</sub>) to induce porosity and microstructure variations. Energy density is calculated as  $E_V = \frac{P}{V \times H \times L} [J \cdot mm^{-3}]$  where  $H = 90 \ \mu m$  and  $L = 30 \ \mu m$  are the hatch spacing and layer thickness, respectively.

To facilitate interpretation, the treatment conditions in Figure 7 are color coded, e.g., the nominal treatment conditions (N) is demarcated in black. The nominal treatment condition (N),

recommended by the machine manufacturer has a laser power P = 230 W,  $V = 1200 \text{ mm} \cdot \text{s}^{-1}$  resulting in  $E_v = 71 \text{ J} \cdot \text{mm}^{-3}$ . In this labeling scheme, the lowest level of laser power  $P_1 = 160 \text{ W}$ , and the highest level  $P_4 = 255 \text{ W}$ . Likewise,  $E_1$  denotes the lowest energy density setting of P = 175 W,  $V = 1400 \text{ mm} \cdot \text{s}^{-1}$  resulting in  $E_v = 46 \text{ J} \cdot \text{mm}^{-3}$ . The applied energy density increases to  $E_4 = 100 \text{ J} \cdot \text{mm}^{-3}$  in which P = 270 W,  $V = 1000 \text{ mm} \cdot \text{s}^{-1}$ . For example, the six overhang parts were manufactured under constant processing conditions and are labeled O- $E_1$ , O- $E_2$ , O-N, O- $E_3$ , and O- $E_4$  with the nominal condition (N) replicated. Likewise, the three psi-shaped parts were also manufactured under constant conditions and are labeled,  $\Psi$ - $E_1$ ,  $\Psi$ -N, and  $\Psi$ - $E_4$ .

Further, for certain parts, the processing conditions are not maintained constant but are changed during processing in an attempt to control the thermal history in the part. For example, one of the two tower geometries, labeled (T-NP<sub>3</sub>P<sub>4</sub>) was manufactured with changing processing conditions, with the first 11 mm (366 layers) under nominal conditions (N), the next 4 mm (133 layers) at treatment condition P<sub>3</sub>, and the last 7 mm (233 layers) under treatment condition P<sub>4</sub>. Similarly, one of the solid vases (VS-NP<sub>2</sub>) and hollow vases (VH-NP<sub>2</sub>), and one of the cones (C-NP<sub>1</sub>) were printed under varying processing conditions. As demarcated in Figure 7, it was observed that setting laser power  $P \le 185$  W and  $E_v \le 57$  J·mm<sup>-3</sup> resulted in lack-of-fusion porosity. In other words, conditions P<sub>1</sub>, P<sub>2</sub>, E<sub>1</sub>, and E<sub>2</sub> cause lack-of-fusion porosity.

Table 1: Nominal processing parameters, material properties and sensor specifications used in this work.

Process Parameter [Units]	Values
Nominal Laser Power, P [W]	230
Nominal Scanning Velocity, V [mm·s <sup>-1</sup> ]	1200
Hatch Spacing, H [mm]	0.09
Layer Thickness, L [mm]	0.03
Volumetric Global Energy Density E <sub>v</sub> [J·mm <sup>-3</sup> ]	71
Build Atmosphere	Argon
Build Plate Preheat Temperature [°C]	50
Recoater Cycle Time [sec]	10
Recoater Blade Type	Metal
<b>Powder Material Properties</b>	Values
Material Type	Inconel 718
Material Manufacturer	Carpenter Addtive
Powder Size Range [µm]	15-45 (D10–D90)
IR Thermal Camera Specifications	Values
Brand and Model	Micro Epsilon – thermoImager Tim 640
Resolution [pixels], [pixels per mm <sup>2</sup> ]	640 × 480 , 10
Frame Rate [Hz]	33
Spectral Rang [µm]	8–14
<b>Optical Tomography Camera Specifications</b>	Values
Brand and Model	Basler acA4024–29 μm
Resolution [pixels], [pixels per mm <sup>2</sup> ]	3036 × 4024 , 346
Frame Rate [Hz]	4
Spectral Rang [nm]	750–1000

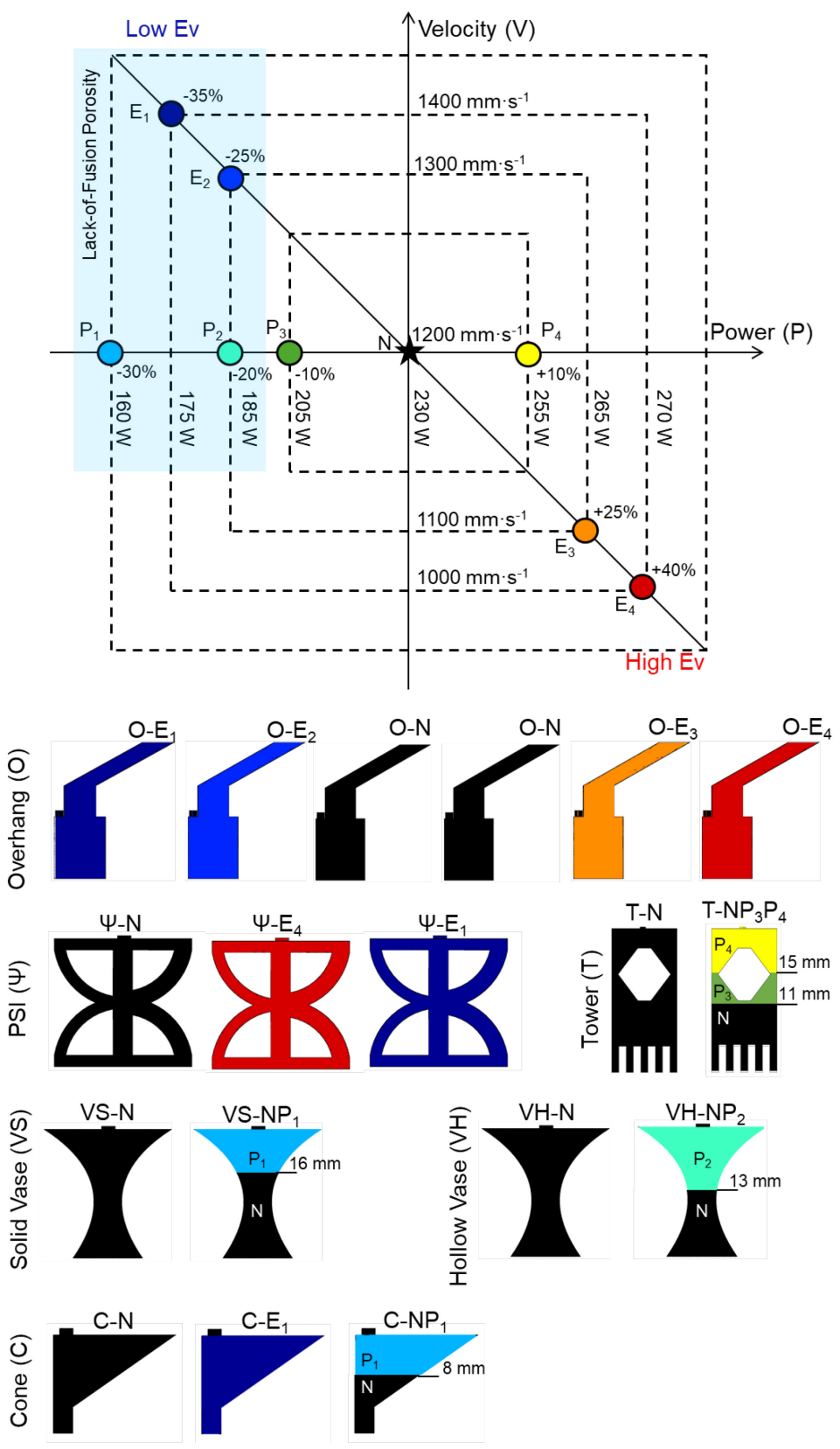


Figure 7: Design of experiments varying laser power (P), scan velocity (V), and processing parameter within a part. The nominal condition is demarcated as N and color coded in black.

#### 3.3 Materials Characterization

After manufacturing, samples were removed from the build plate using wire electrical discharge machining, cross-sectioned, and mounted in graphite infused resin for microstructural characterization. The samples were successively ground using 300, 480, 600, 800, and 1200 grit polishing pads, and polished to mirror finish using 50 nm silica suspension.

# 3.3.1 Porosity

To discern the occurrence of lack-of-fusion porosity, the samples were examined using optical microscopy (Keyence VK-X3000). All 18 samples were assessed for porosity, of these, 7 samples depicted lack-of-fusion porosity. The samples with lack-of-fusion porosity were:  $\Psi$ -E<sub>1</sub>, VS-NP<sub>1</sub>, VH-NP<sub>2</sub>, C-E<sub>1</sub>, C-NP<sub>1</sub>, O-E<sub>1</sub>, and O-E<sub>2</sub>. Shown in Figure 8(a) is a stitched optical microscopy image for  $\Psi$ -E<sub>1</sub>. The optical micrograph depicts significant occurrence of lack-of-fusion porosity with its characteristic non-circular, jagged edge with a high aspect ratio noted in Figure 8(b) [46]. The lack-of-fusion pores observed in this work typically exceeded 100  $\mu$ m in diameter. Further examination of individual lack-of-fusion pores with scanning electron microscopy (SEM, JEOL IT-500HR), exemplified in Figure 8(c), revealed the presence of unmelted powder. Indeed, all processing conditions where laser power P  $\leq$  185 W, viz., 20% reduction in laser power from nominal P = 230 W, resulted in lack-of-fusion porosity. Keyhole melting and gas porosity were not observed in any of the samples.

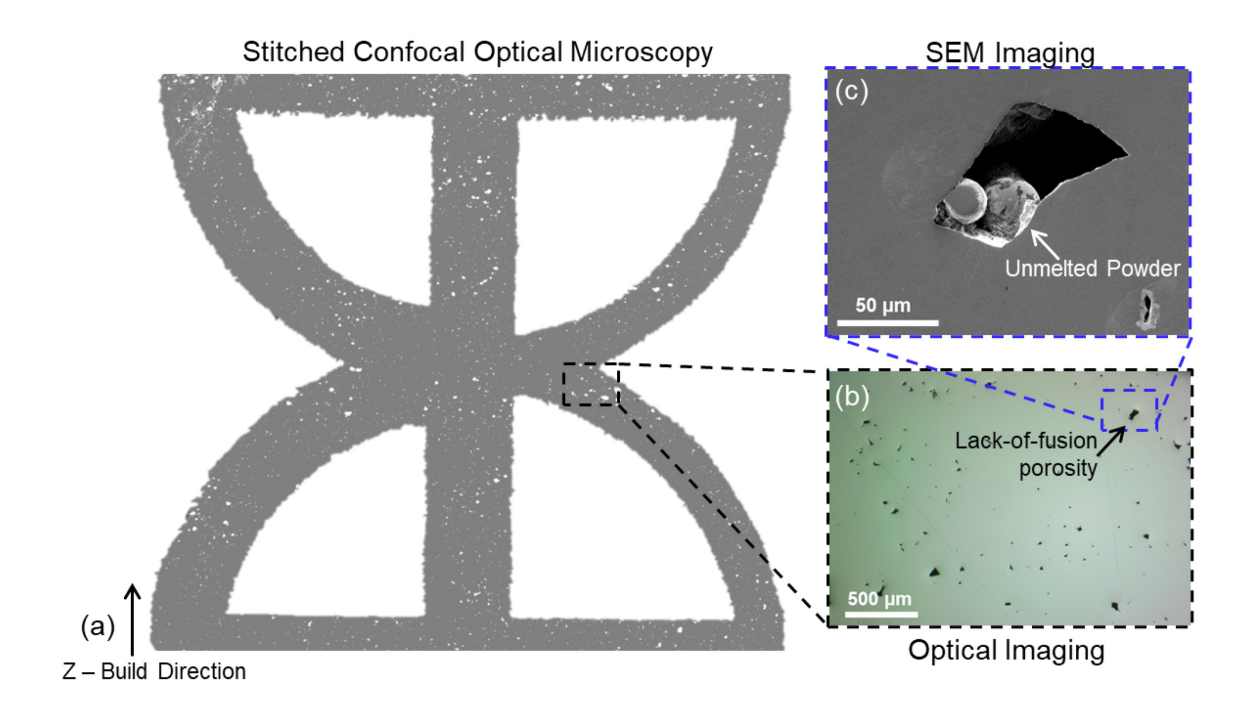


Figure 8: Lack-of-fusion porosity characterized using optical and scanning electron microscopy (SEM). (a) Stitched confocal microscopy image of the psi-shaped part  $\Psi$ -E<sub>1</sub>, along with (b) optical and (c) SEM images. Considerable lack-of-fusion porosity of size > 100  $\mu$ m is observed when laser power  $P \le 185$  W.

# 3.3.2 Meltpool Depth $(d_p)$

To determine meltpool depth  $(d_p)$ , the samples devoid of lack-of-fusion porosity were chemically etched with aqua regia (3:1 = HCl:HNO<sub>3</sub>). In total 10 samples were measured for meltpool depth analysis. Subsequently, images of the cross-section, as shown in Figure 9, were acquired with optical microscopy. In Figure 9 the laser moves in and out of the plane of the page.

The meltpool depth  $(d_p)$  was measured in accordance with NASA MSFC-SPEC-3717 [48]. Shown in Figure 9 are meltpool measurements for  $\Psi$ -E<sub>1</sub>,  $\Psi$ -N, and  $\Psi$ -E<sub>4</sub>. Large variation in the meltpool depth  $(d_p)$  between parts processed under identical conditions is considered an indicator of process instability. This specification instructs that the meltpool depth should only be measured with reference to the topmost surface, and not at the preceding layers. This is because the laser remelts the previous layers, hence the datum is lost. The meltpool depth quantifies the penetration

of the laser into previous layers. Between 2 to 3 layers of penetration, viz., in this work,  $d_p = 60$  to 90  $\mu$ m with L = 30  $\mu$ m, is considered ideal for obtaining dense samples without porosity. An ideal degree of meltpool penetration is observed for  $\Psi$ -N. A shallower penetration indicates insufficient melting, while deeper penetration is correlated with occurrence of keyhole porosity and grain coarsening [86]. The penetration of  $\Psi$ -E<sub>1</sub> is less than 2 layers; this sample had substantial lack-of fusion porosity as observed in Figure 8. A total of 515 measurements of meltpool depth were obtained.

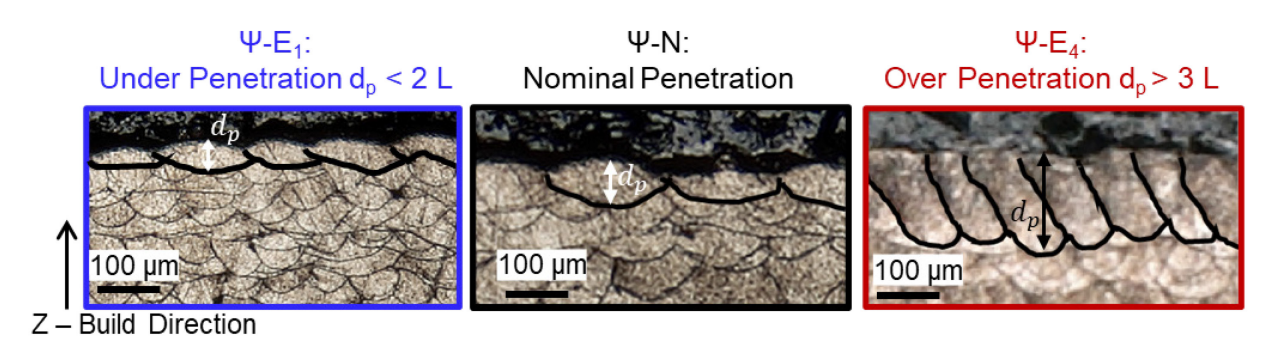


Figure 9: Meltpool depth  $(d_p)$  measured in samples  $\Psi$ - $E_1$ ,  $\Psi$ -N, and  $\Psi$ - $E_4$ . based on the NASA MSFC-SPEC-3717. Sample meltpool depths are shown for (a)  $\Psi$ - $E_1$ , (b)  $\Psi$ -N, and (c)  $\Psi$ - $E_4$ . The laser scans each hatch perpendicular to the plane of the page.

# 3.3.3 Grain Size (Primary dendritic arm spacing, PDAS, $\lambda_1$ )

Consistent with prior findings concerning LPBF of Inconel 718, all parts in this work portrayed columnar dendritic-type microstructure [3, 4, 28]. Consequently, the grain size is assessed in terms of the primary dendritic arm spacing ( $\lambda_1$ ). Depending on the part geometry, the grain size was measured at 10 to 12 sample locations as depicted in Figure 10. These measurement locations were selected to assess the effect of thermal history at certain regions where heat retention would lead to microstructure heterogeneity, e.g., overhang regions and around cavities. At each of the annotated locations in Figure 10, two SEM images were obtained. Within each SEM image, the grain size was measured at 2 sample locations, using the industry standard bounding

box procedure discussed in our pervious work [81]. A total of 852 individual measurements of grain size were obtained.

#### 3.3.4 Microhardness

Microhardness measurements were acquired at the same locations as SEM images for grain size, depicted in Figure 10. At each location, five Vickers microhardness indentations (Buehler Wilson VH1102) were conducted at 0.3 kgf in the standard star indentation pattern for a duration of 10 seconds (Hv<sub>0.3,10</sub>). These five microhardness indentations were averaged per each measurement location. In all, 1,065 individual hardness measurements were acquired.

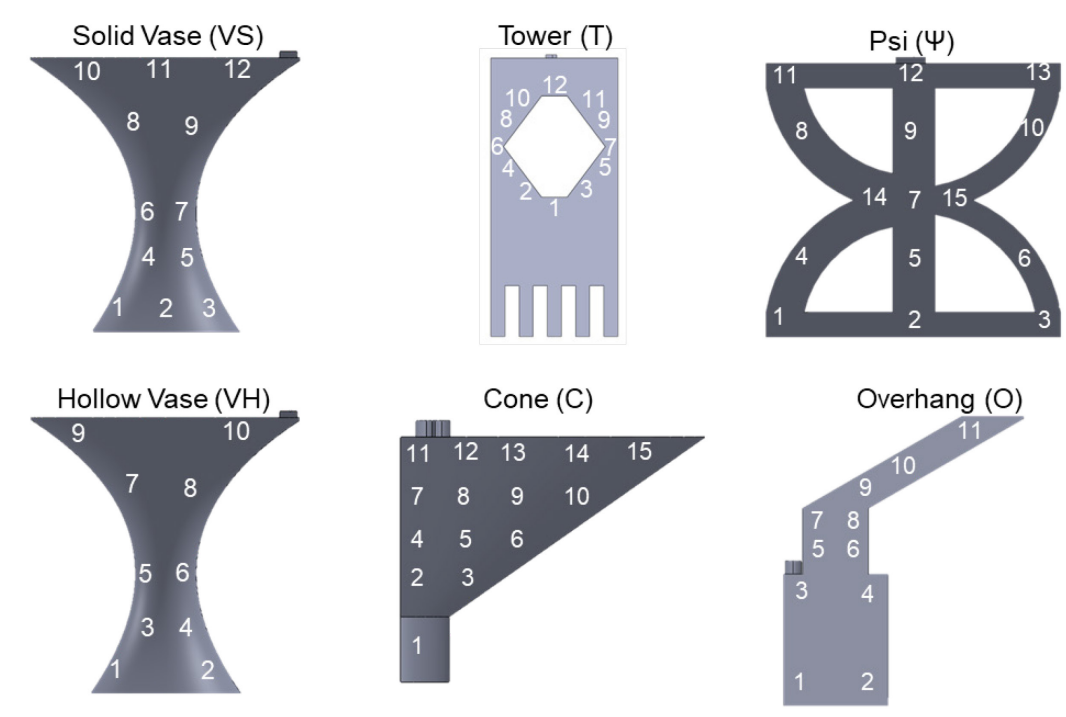


Figure 10: Locations of grain size (SEM) and microhardness measurements for 6 part geometries. Two SEM images and five microhardness indentations were taken per location. A total of 10 parts without lack-of-fusion porosity were assessed; 852 grain size and 1,065 individual microhardness readings were acquired.

# 4 Digital Twin Modeling

#### 4.1 Sensor Signatures

Three process signatures are extracted from the data acquired by the infrared and optical cameras. These are the end-of-cycle temperature ( $T_e$ , [ $^{\circ}$ C]), meltpool intensity ( $I_m$ , [unitless]), and inter-layer time ( $t_l$ , [s]). Each of these is described herewith, noting that the data from the sensors are synchronized.

# 4.1.1 End-of-cycle Temperature (T<sub>e</sub>)

The data from the LWIR thermal camera is processed to extract the end-of-cycle temperature (Te, [°C]). Shown in Figure 11(a) is the as-received LWIR image at layer 20. A zoomed in section of the temperature history data is shown in Figure 11(b), where the end-of-cycle temperature for the observed pixel location is demarcated with a red dot. The end-of-cycle temperature is essentially the minimum temperature attained at a location prior to the commencement of laser melting. In Figure 11(c), the end-of-cycle temperatures for all pixel locations are consolidated over an entire layer to generate a layer-wise 2D image. Figure 11 (d-f) shows the change in end-of-cycle temperature for 3 select layers; note the heat retention in certain samples.

In Figure 12, the end-of-cycle (T<sub>e</sub>) images in Figure 11 are rendered in 3D for all layers of the build. In this 3D rendering the effect of part shape on T<sub>e</sub> is evident. For example, comparing the psi (Ψ-N), vase (VS-N), overhang (O-N), and cone (C-N) geometries processed under identical nominal parameter conditions, C-N and VS-N tend to retain significantly more heat near the top layers compared to Ψ-N and O-N.

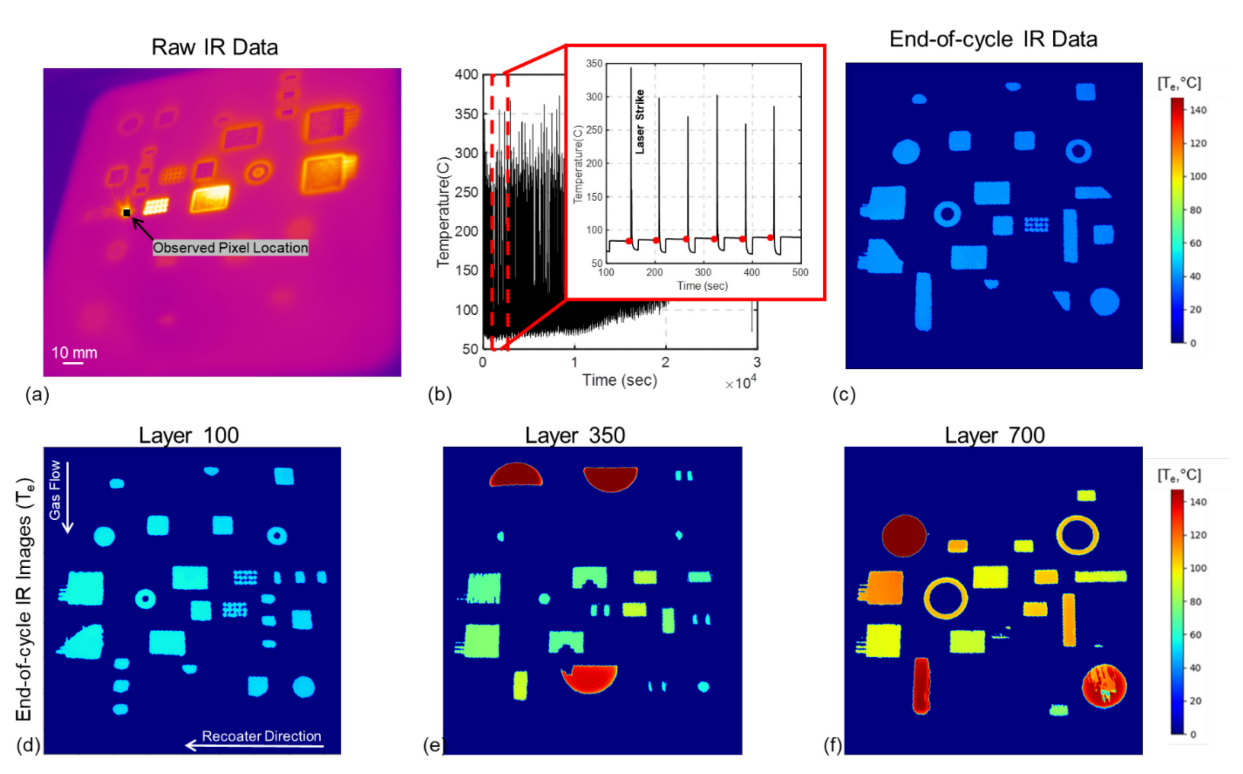


Figure 11: (a) As-received thermal imaging data is converted to (b) point-wise and (c) 2D image representation of end-of-cycle temperature  $(T_e)$ . (d-f) 2D  $T_e$  images for three representative layers.

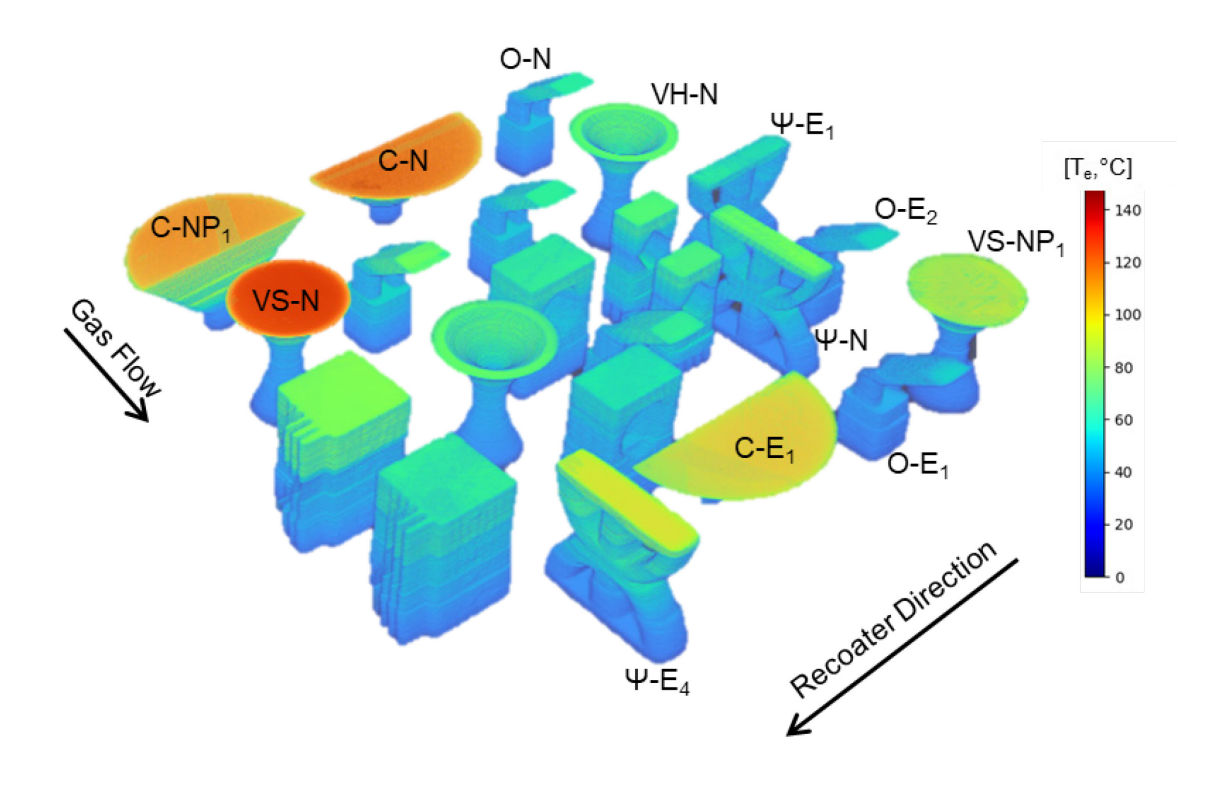


Figure 12: 3D rendering of the end-of-cycle (Te) images. Prominent variation in thermal history is observed contingent on the part geometry. Note the difference between C-N, VS-N, and O-N.

# 4.1.2 Meltpool Intensity (Im)

The optical tomography camera captures light emitted at wavelengths > 750 nm over a 250 ms exposure time. This long exposure allows the optical camera to detect the most intense light emitted in the near infrared regime at each pixel. We extract this maximum light intensity recorded at each pixel and term this feature as the meltpool intensity ( $I_m$ ). This corresponds to the instant when the laser interacts with the metal powder.

Exemplified in Figure 13 is the meltpool intensity for each pixel for four representative layers. A prominent variation in the meltpool intensity is evident between identically-shaped parts processed under different conditions, for example, note the difference in I<sub>m</sub> over time (layers) for the overhang parts O-N, O-E<sub>1</sub>, and O-E<sub>3</sub>. Further, I<sub>m</sub> also changes between parts of different shapes processed under identical conditions, as observed in C-N, VS-N, and O-N. A 3D rendering of the meltpool intensity images (I<sub>m</sub>) is shown in Figure 14.

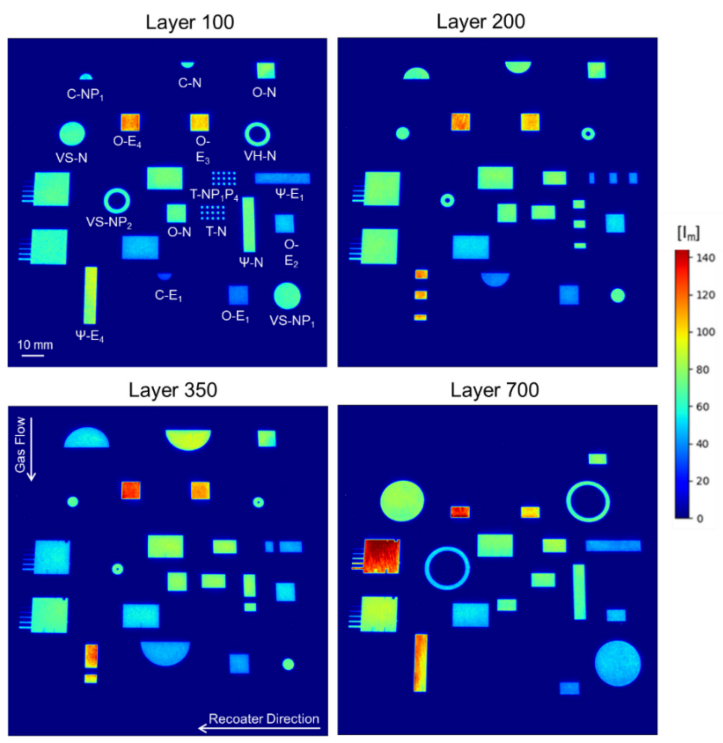


Figure 13: The meltpool intensity ( $I_m$ ) images obtained from the optical tomography camera. Note the difference between O-N, O-E<sub>1</sub>, and O-E<sub>4</sub>.

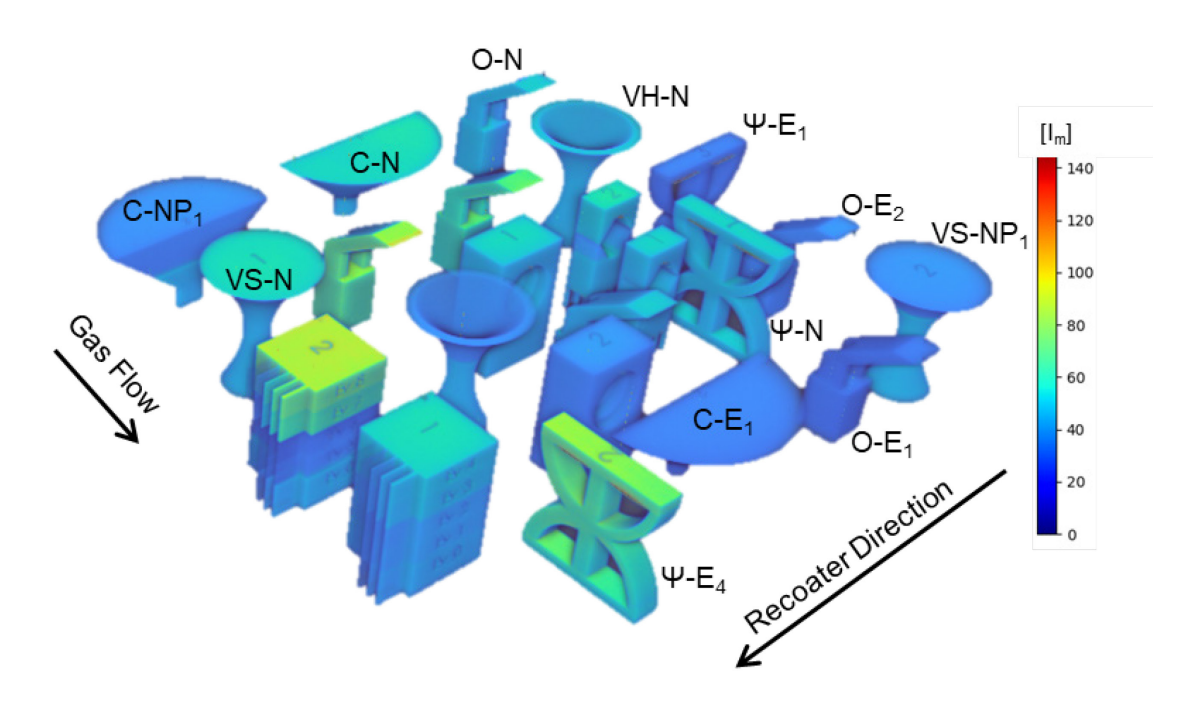


Figure 14: 3D rendering of the meltpool intensity  $(I_m)$  for the entirety of the build. The meltpool intensity  $(I_m)$  is primarily influenced by the processing parameters.

Continuing with the analysis, in Figure 15, the *layer-average* end-of-cycle temperature ( $T_e$ ) and *layer-average* meltpool intensity ( $I_m$ ) are mapped for the three psi-shaped parts  $\Psi$ - $E_1$ ,  $\Psi$ -N,  $\Psi$ - $E_4$ . We note that substantial lack-of-fusion porosity was observed in  $\Psi$ - $E_1$ . In Figure 15(b) the average end-of-cycle temperature ( $T_e$ ) for each layer not only varies between the different processing conditions, but also changes between layers of the same part on account of its changing cross-section. In contrast, in Figure 15(a) the mean layer intensity ( $I_m$ ) responds to change in processing conditions more than the effect of part geometry. Thus, compared to the end-of-cycle temperature ( $T_e$ ), the meltpool intensity ( $I_m$ ) is less responsive to the change in part shape. However, as evident from comparison of  $\Psi$ -N and  $\Psi$ - $E_1$ ,  $I_m$  varies to a greater magnitude with change in input energy compared to  $T_e$ . Similar trends were observed for other part geometries.

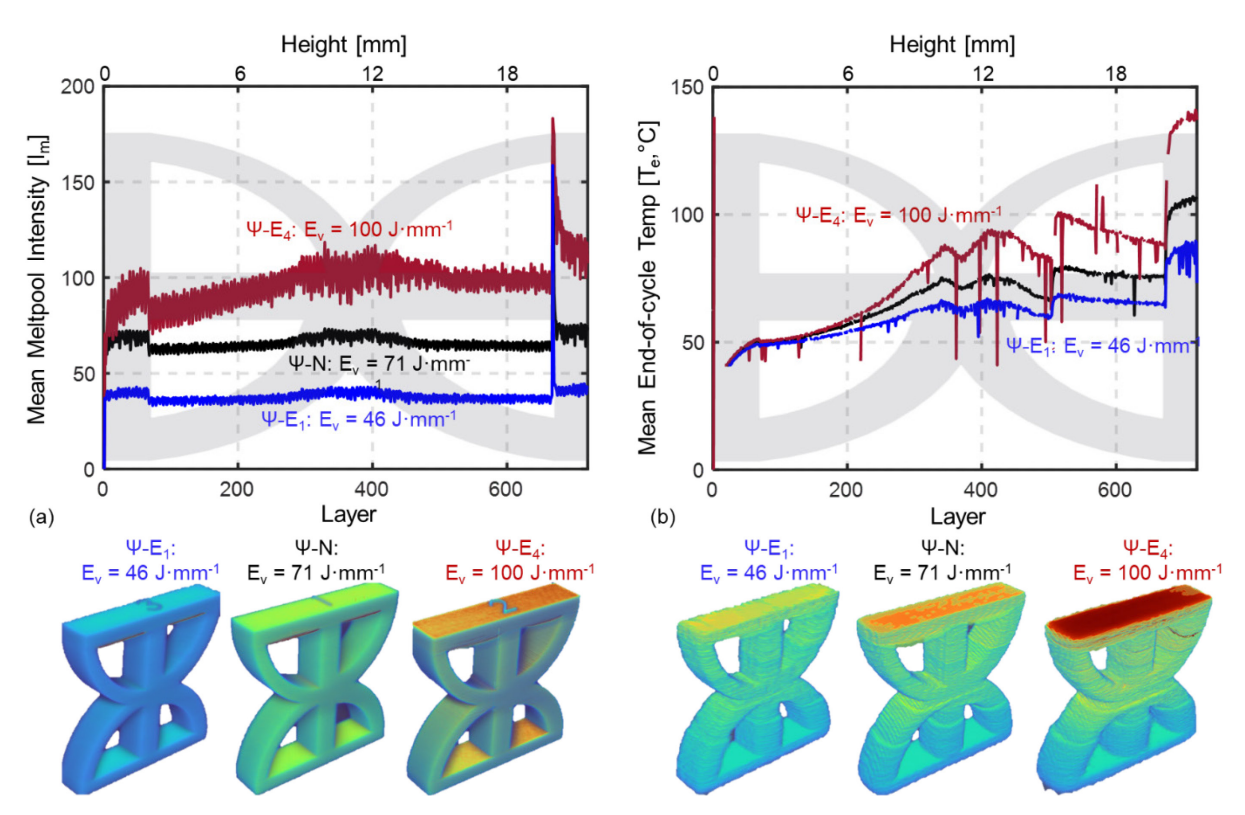


Figure 15: Layer-wise sensor signatures for the three psi geometries,  $\Psi$ -E<sub>1</sub>,  $\Psi$ -N,  $\Psi$ -E<sub>4</sub>. (a) change in meltpool intensity ( $I_m$ ). (b) end-of-cycle temperature ( $T_e$ ). The meltpool intensity ( $I_m$ ) responds to processing parameters while the end-of-cycle temperature ( $T_e$ ) is influenced by change in the layer-by-layer cross-section.

#### 4.1.3 Inter-layer time (t<sub>1</sub>)

A third sensor signature called the inter-layer time (t<sub>I</sub>, [s]) is derived from the time synchronized T<sub>e</sub> and I<sub>m</sub> data. A representative cooling curve for a layer is shown in Figure 16. The peak of this curve corresponds to the meltpool intensity (I<sub>m</sub>) at the instant of the laser strike acquired from the optical tomography camera. The bottom of the cooling curve is the end-of-cycle temperature (T<sub>e</sub>) observed from the thermal camera. From the time stamp of the I<sub>m</sub> data the approximate instant of the laser strike for a location is obtained. Likewise, the time stamp of T<sub>e</sub> images provides the moment when the end-of-cycle temperature is attained. The inter-layer time (t<sub>I</sub>) is the duration between the peak of the laser strike to the end-of-cycle temperature of the cooling curve.

Visualized in Figure 17 is the inter-layer time ( $t_I$ ) for every layer of the build. Changes in the inter-layer time ( $t_I$ ) are caused by changes in the surface area of the build. For example, at 15 mm (500 layers) of build height, the three cone geometries are completed and the inter-layer time ( $t_I$ ) decreases from  $\sim 37$  s to  $\sim 24$  s.

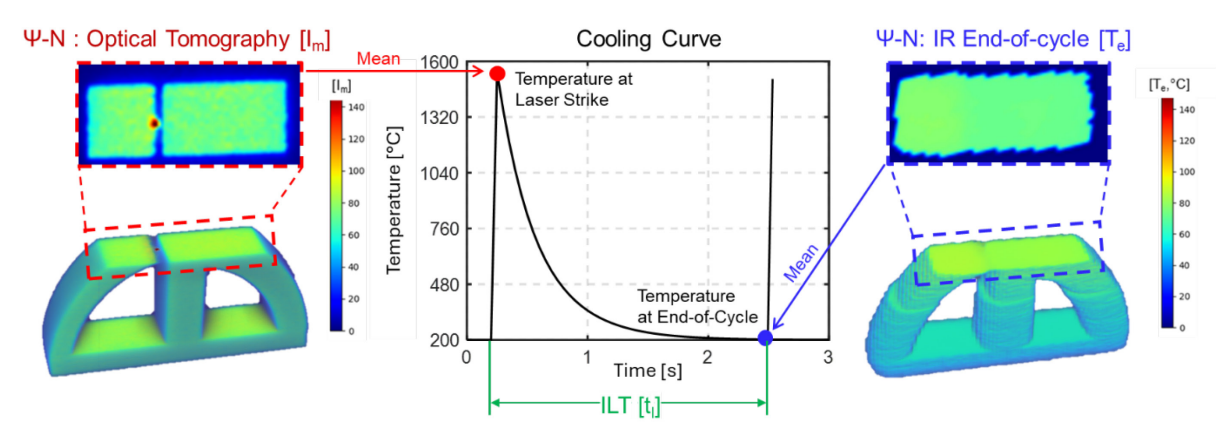


Figure 16: The approach to obtain the inter-layer time ( $t_l$ ) with the aid of optical tomography and thermal imaging data. The instant where the cooling curve peaks is captured by  $I_m$  and the end-of-cycle temperature is represented with  $T_e$ . The inter-layer-time ( $t_l$ ) is the duration between the peak ( $I_m$ ) and end-of-cycle temperature ( $T_e$ ).

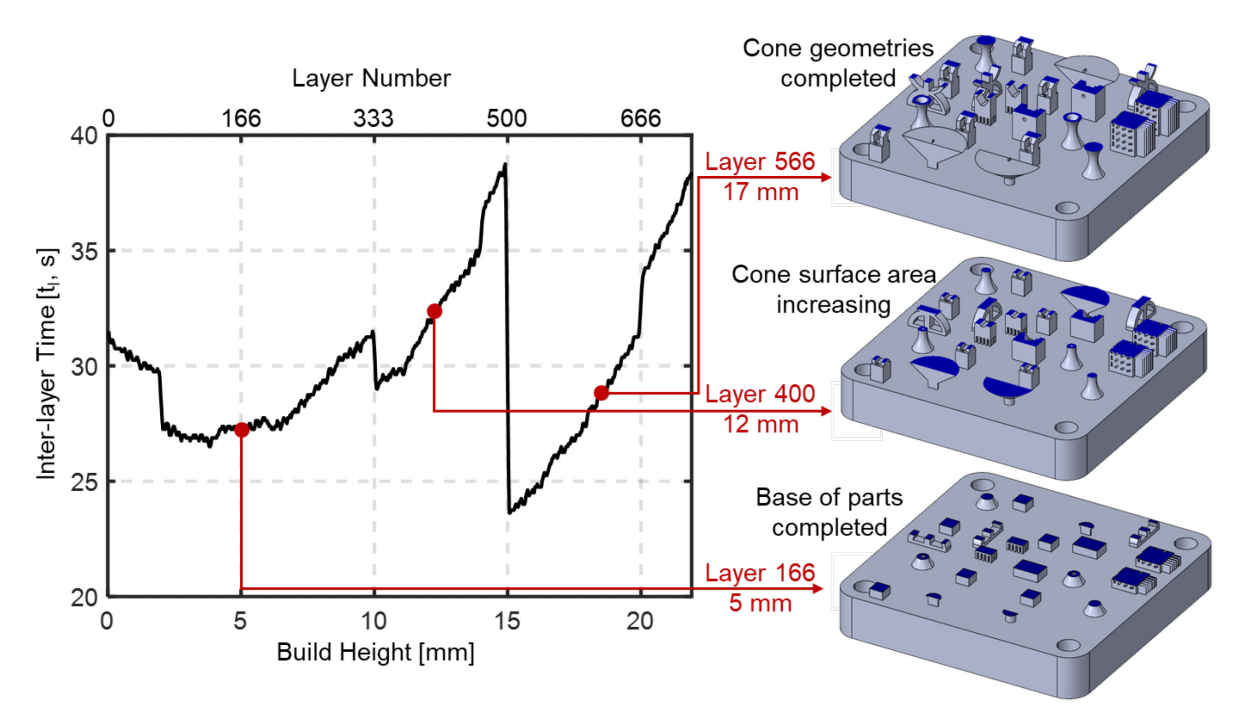


Figure 17: Inter-layer time (tI) is extracted for all layers in the build, in which the cross-sectional area directly impacts the time taken for cooling.

# 4.2 Thermal Modeling

# 4.2.1 Background

The thermal history T(x, y, z, t) of an LPBF part is the temperature T at every location (x,y,z) at time (t). The thermal history of a part is a function of its material properties, geometry, and processing parameters, and is obtained by solving the heat diffusion equation, Eq. (1) [87, 88].

$$\frac{\text{Material Properties}}{\widetilde{\rho c_p}} \frac{\partial T(x, y, z, t)}{\partial t} - k \underbrace{\left(\frac{\partial^2}{\partial x^2} + \frac{\partial^2}{\partial y^2} + \frac{\partial^2}{\partial z^2}\right)}_{\text{Shape of the Part}} \underbrace{\frac{Part}{Temperature}}_{\text{Temperature}} = Q \tag{1}$$

In the heat diffusion equation, the material properties are assumed constant and consist of the bulk material density,  $\rho$  [kg·m<sup>-3</sup>]; specific heat capacity,  $c_p$  [J·kg<sup>-1</sup>·K<sup>-1</sup>]; thermal conductivity, k [J·s<sup>-1</sup>·m<sup>-1</sup>·K<sup>-1</sup>]; volumetric heat flux, Q [W·m<sup>-3</sup>] viz., is the magnitude of heat supplied per second to melt a unit volume of the material. The volumetric heat flux  $Q = \frac{P}{V \cdot H \cdot L \cdot t_q}$  is a function of the LPBF process parameters: laser power (P, [W]), scan speed (V, [m·s<sup>-1</sup>]), hatch spacing (H, [m], layer thickness (L, [m]), and active laser time (t<sub>q</sub>, [s]), which is the length of time that the laser is on while generating the fixed volumetric heat flux. The second derivative in Eq. (1) is called the continuous Laplacian operator and captures the effect of part shape.

The finite element (FE) method is the most common approach used to solve the heat diffusion equation [88, 89]. A computational disadvantage of using FE analysis for predicting the thermal history in LPBF is that the part geometry has to be repeatedly remeshed to account for its changing cross-section with the deposition of each new layer [34, 89, 90]. It takes hours if not days to ascertain the thermal history of practical LPBF parts [32-34]. To overcome this computational disadvantage, commercial FE-based simulation packages have advanced adaptive meshing

techniques [88, 91]. In adaptive meshing the element size changes continually, with location-specific mesh coarsening and refinement between time steps. This variation in element size impacts the prediction accuracy of cooling rates and end-of-cycle temperature.

To overcome the shortcomings of FE-based analysis, in this work we use a rapid and meshless graph theory-based approach to predict the thermal history [24, 27, 81, 92-94]. The approach, summarized in Figure 18, is a discrete, mesh-free method to rapidly solve the heat diffusion equation [92]. The graph theory approach, which has been experimentally validated in our previous work, is found to 10 to 20-times faster than research-based FE analysis with accuracy within 5% of observed surface temperature distribution [24, 81, 92]. Additionally, the temperature and cooling rate at each node can be readily probed and tracked with the graph theory model. In contrast, commercial FE-based simulation software is typically user-locked and only outputs visualizations of the simulated results. By implementing the graph theory model, the thermal history was predicted between 6 minutes (hollow vase) and 38 minutes (cone) depending on the part volume.

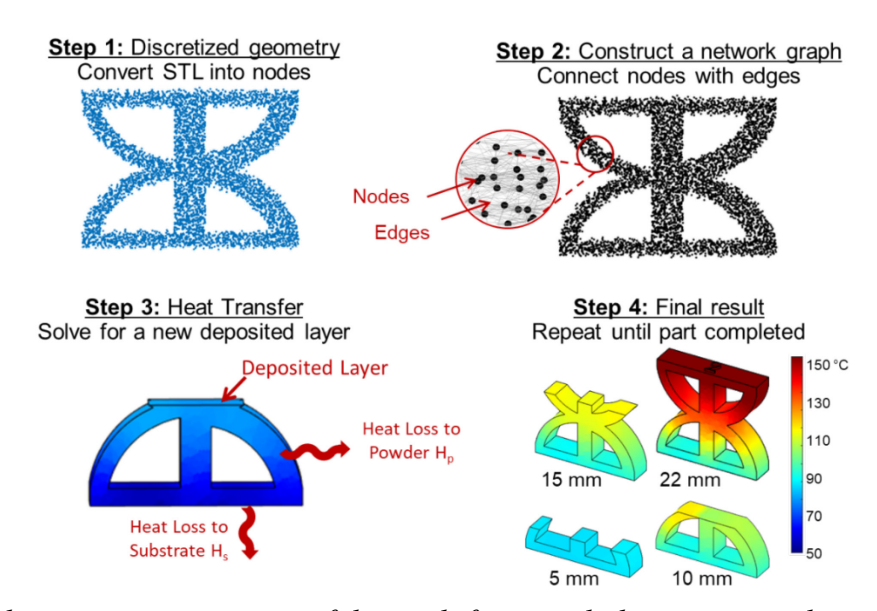


Figure 18: A schematic representation of the mesh-free graph theory approach used in this study to simulate the thermal history. Shown here is the example of the psi geometry.

In the graph theory approach, the temperature distribution T(x, y, z, t) in Eq. (2) is solved as a function of the eigenvectors ( $\phi$ ), and eigenvalues ( $\Lambda$ ) of the Laplacian Matrix (L) over the discrete nodes [94]. The approach provides a semi-analytical solution to the heat diffusion equation shown in Eq. (2).

$$T(x, y, z, t) = \Phi e^{-\frac{k}{\rho c_p} g \Lambda t} \Phi' \left( \frac{A_e S_l}{\rho v c_p} \frac{P}{V} + T_{prev} \right)$$
 (2)

In Eq. (2), the effective laser absorptivity is denoted by  $A_e$ ; volume of melted material v [mm<sup>3</sup>]; total length scanned per layer  $S_l$  [mm]; scan speed as V [mm·s<sup>-1</sup>]; laser power P [W]; and temperature of the previously deposited layer predicted  $T_{prev}$  [°C]. A non-dimensional constant g = 0.6 is used as a scaling factor. For this work  $A_e$  = 0.60 based on experiments conducted by Ye et. al. [95].

To facilitate rapid convergence, a meta-layer or super-layer modeling approach is used, wherein deposition of several layers is simulated at once – as commonly implemented in commercial and research-based FE approaches [89]. In this work, the super-layer size is 5 layers (150 μm). These and other model parameters are listed in Table 2. *The resolution and accuracy of the model is contingent on the node density, i.e., number of nodes per unit volume, in this work the node density is maintained in the range of 4 to 7.5 nodes per mm<sup>3</sup>. A higher node density is needed for larger volume parts. A higher node density improves model accuracy at the expense of computation time; the relationship is O<sup>3</sup>.* 

The thermal model considers the material properties, such as specific heat to be temperature independent and ignores the effect of phase change and latent heat of melting. These materials properties are listed in Table 2 and considered at 50% of the melting point of the material. The errors due to maintaining material properties fixed is compensated by calibrating the boundary

conditions (explained in forthcoming Sec. 4.2.2). Since the end of cycle temperature and cooling time occur below the melting point of the material, the effects of latent heat and phase change are further mitigated.

Table 2: Simulation parameters obtained after model calibration

Simulation Parameters	Values
Heat loss coefficient part to powder, h <sub>p</sub> [W·m <sup>-2</sup> · °C]	30
Heat loss coefficient part to substrate, h <sub>s</sub> [W·m <sup>-2</sup> · °C]	8,000
Heat loss coefficient to gas flow, hg [W·m <sup>-2</sup> · °C]	<mark>60</mark>
Thermal Conductivity (k) [W·m <sup>-1</sup> .°C]	19.47
Density (ρ) [kg·m <sup>-3</sup> ]	8,193
Specific Heat (c <sub>p</sub> ) [J·Kg <sup>-1</sup> ·°C <sup>-1</sup> ]	<mark>626</mark>
Melting Point [°C]	1,609
Ambient chamber temperature [°C]	<mark>50</mark>
Node density [nodes·mm <sup>3</sup> ]	4 to 7.5
Superlayer thickness [mm]	0.15 (5 actual layers)
Gain factor (g) [unitless]	0.6
Computational hardware	Intel(R) Core(TM) i9-9900K CPU, @
	3.60 GHz

# 4.2.2 Thermal History Quantifiers

Two quantifiers of the part-scale thermal history were derived from the graph theory thermal model, namely, the end-of-cycle temperature ( $\widehat{T}_e$ ), [°C] and cooling time ( $\widehat{t}_c$ ), [s]. In our previous works, the grain size and meltpool depth were correlated to  $\widehat{T}_e$  and  $\widehat{t}_c$  [81]. From a metallurgical perspective, these are analogous to thermal gradient (G, °C·m<sup>-1</sup>) and solidification velocity (R, m·s<sup>-1</sup>) respectively [5]. The end-of-cycle temperature ( $\widehat{T}_e$ ) predicted from the thermal model is the counterpart to the end-of-cycle surface temperature ( $T_e$ ) observed from the thermal camera.

(a) End-of-cycle temperature ( $\hat{T}_e$ ), and Model Calibration and Validation

The average top surface end-of-cycle temperature predicted by the thermal model  $(\hat{T}_e)$  is calibrated with the extracted average top surface end-of-cycle temperature  $(T_e)$  observed from the thermal camera. First, the nominal solid vase (VS-N) was used to calibrate the boundary conditions and heat loss coefficients of the graph theory model [27]. The calibrated model

parameters were subsequently used for all other parts. The procedure for model calibration is summarized in our prior publications [24, 27], and briefly summarized herewith.

Three heat transfer-related boundary conditions were calibrated (Table 2): (i) heat loss from the part to the build plate (h<sub>s</sub>); (ii) heat loss by radiation and forced convection to the gas (h<sub>g</sub>); and (iii) heat loss to the surrounding powder (h<sub>p</sub>) [93, 94]. Heat losses are considered in the graph theory thermal simulation by adjusting the Laplacian matrix with type 3 (convection) boundary conditions [93, 94]. These boundary conditions, listed in Table 2, are calibrated by comparing the model-predicted top surface temperature to experimentally obtained measurements from the IR thermal camera. The IR camera was calibrated using reference thermocouple measurements as described in our previous works [24, 27].

In Figure 19 the end-of-cycle temperature ( $\hat{T}_e$ ) for VS-N predicted by the graph theory model is overlaid on the end-of-cycle temperature ( $\hat{T}_e$ ) measured from the thermal camera. The mean average percentage error (MAPE) and root mean squared error (RMSE) of the predicted  $\hat{T}_e$  with respect to  $\hat{T}_e$  are within 6% and 11 °C, respectively. For VS-N part the graph theory simulation was completed within 9 minutes. The accuracy of the thermal model is further affirmed in the context of  $\Psi$ -E4 and  $\Psi$ -E1. Shown in Figure 20(a) and (b) are the predicted ( $\hat{T}_e$ ) and observed ( $\hat{T}_e$ ) end-of-cycle temperatures for  $\Psi$ -E4 and  $\Psi$ -E1, respectively. These parts were simulated with identical parameters obtained from the calibration step for VS-N. For both parts MAPE was < 5.5%, and the simulation required less than 10 minutes to complete per part. The error between the model-predicted  $\hat{T}_e$  and observed  $T_e$  shown in Figure 20(a) and (b) is likely due to stochastic machine level effects, such as effect of gas flow, uneven recoating, and location-related variation in heating of the substrate. Thus, it is important to monitor both physical model predictions with real-time observations.

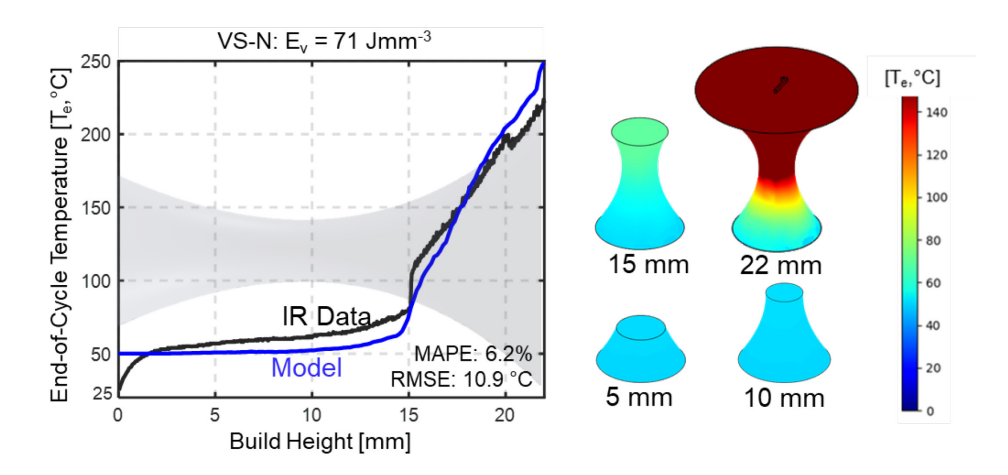


Figure 19: Model calibration. The predicted end-of-cycle temperatures ( $\hat{T}_e$ ) from the thermal model compared to the end-of-cycle temperature measurements ( $T_e$ ) observed from the thermal camera for the solid vase (VS-N). The heat loss parameters in the graph theory were calibrated. The model converged within 9 minutes with MAPE < 7%.

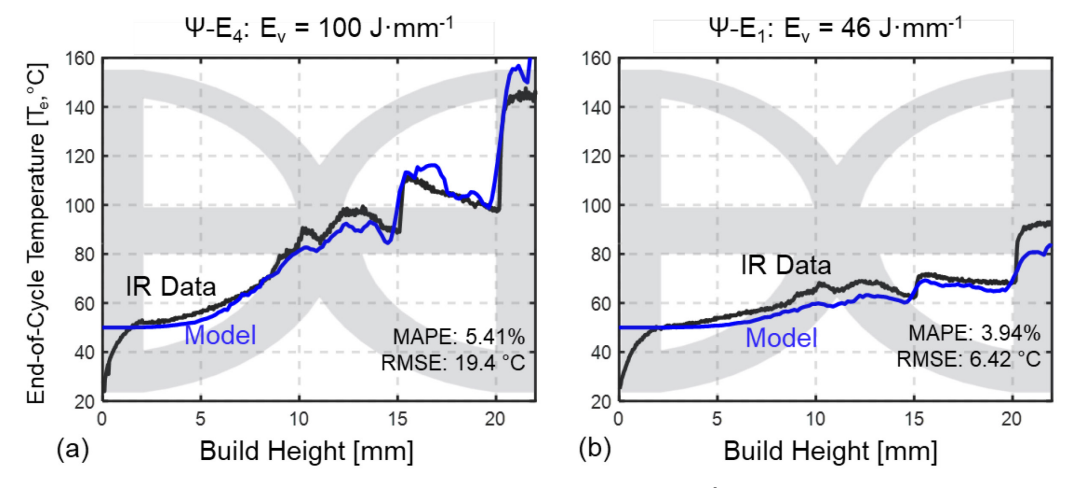


Figure 20: Model validation. The end-of-cycle temperature ( $\hat{T}_e$ ) from the thermal model compared to the end-of-cycle temperature measurements ( $T_e$ ) observed from the thermal camera for the two psi-shaped parts  $\Psi$ -E4 and  $\Psi$ -E1 manufactured under different processing conditions. The model parameters are not changed from the calibration step. The model converges within 10 minutes with MAPE < 5.5%

# (b) Cooling time $(\hat{t}_c)$ ,

From the graph theory-based part thermal history predictions, a metric termed cooling time  $\hat{t}_c$  [s] is extracted for every layer [81]. Shown in Figure 21(a) is the cooling curve obtained from the graph theory model. As demarcated in Figure 21(a), the cooling time ( $\hat{t}_c$ ) is the duration for the temperature to reach 700 °C from its peak at the instant of laser strike. The 700 °C temperature threshold was chosen as it is approximately  $0.5\times$  the melting temperature of Inconel 718, which

has a wide liquidus ranging from 1260 to 1330 °C [28]. The rationale is that repeated heating below 700 °C is unlikely to change the microstructure characteristics, such as grain size [86]. In our previous works, a longer cooling time ( $\hat{t}_c$ ) was found to be positively correlated with grain coarsening and increase in primary dendritic arm spacing ( $\lambda_1$ ) [81].

The cooling time ( $\hat{t}_c$ ) for the three psi-shaped geometries  $\Psi$ -N,  $\Psi$ -E<sub>4</sub> and  $\Psi$ -E<sub>1</sub> are plotted in Figure 21(b). The cooling time increases in proportion to the input energy density, indicating the propensity for heat retention in the sample. Further, the cooling time increases sharply at the overhang regions  $\Psi$ -N and  $\Psi$ -E<sub>4</sub> on account of impeded heat flux through the thin walls (layer 667) and powder trapped underneath. A relatively constant cooling time  $\hat{t}_c$  < 0.3 s is predicted for  $\Psi$ -E<sub>1</sub>, noting that this sample has considerable lack-of-fusion porosity, as first shown in Figure 8.

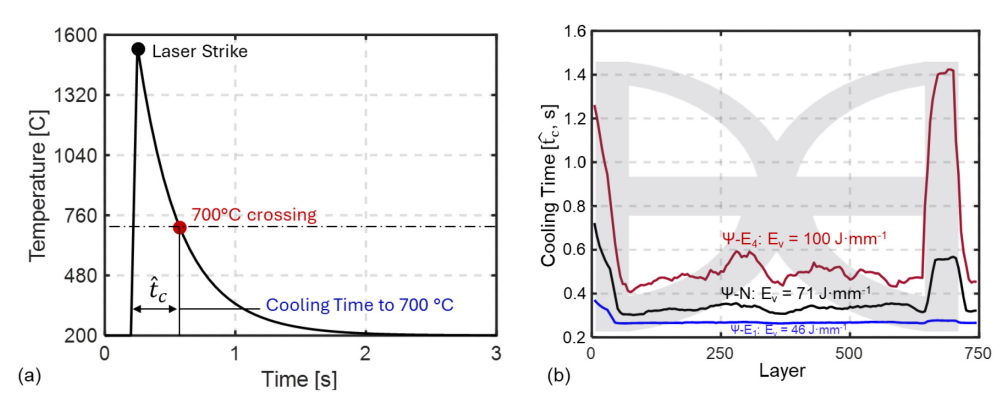


Figure 21: (a) Procedure for estimation of the cooling time ( $\hat{t}_c$ ) from the cooling curve obtained from the thermal model. (b) Cooling time for each layer of the three psi-shaped geometries  $\Psi$ -N,  $\Psi$ -E<sub>4</sub> and  $\Psi$ -E<sub>1</sub>. Cooling time increases with input energy ( $E_v$ ) due to heat retention. Cooling time for  $\Psi$ -E<sub>1</sub> was the lowest, and almost constant throughout and had extensive lack-of-fusion porosity.

## 4.3 Machine Learning

# 4.3.1 Model Architecture

A hierarchical machine learning architecture, shown in Figure 22, is used for assessing the part quality. The first echelon of the model discerns between parts with and without lack-of-fusion porosity. The next echelon concerns prediction of the meltpool depth  $(d_p)$ , grain size  $(\lambda_1)$ , and

microhardness (Hv). A hierarchical approach is implemented because the presence of lack-offusion porosity in parts for safety-critical applications is considered unacceptable, and the parts are often rejected [96]. Hence, it would be impractical to predict microstructure evolution in samples with lack-of-fusion porosity. We note that the first echelon is a classification-type machine learning problem as its aim is to distinguish between porosity and no-porosity conditions. The second echelon is a regression problem, as the aim is to predict the value of  $d_p$ ,  $\lambda_1$ , and Hv.

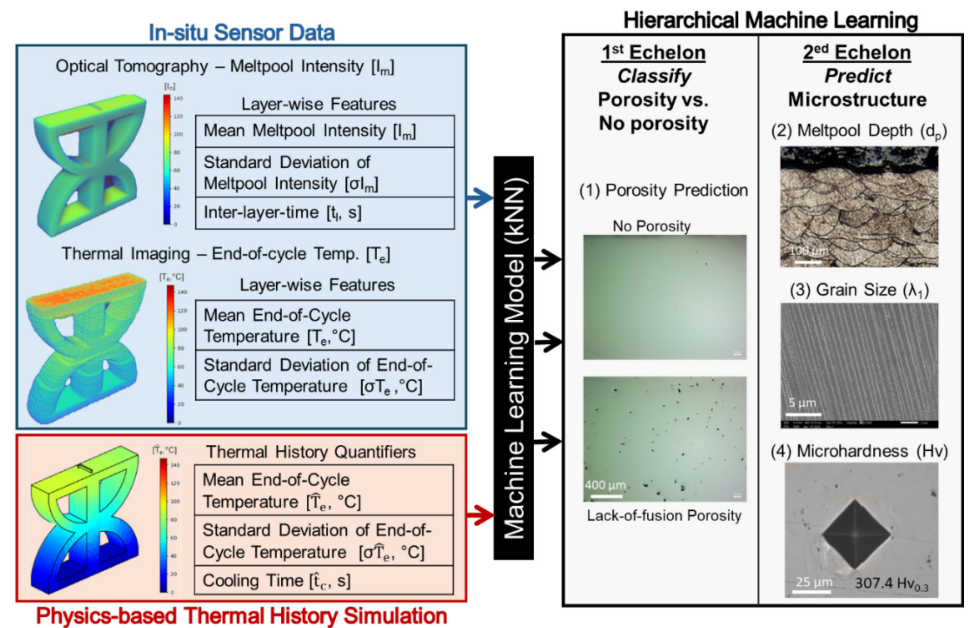


Figure 22: Schematic of the hierarchical machine learning approach used for the digital twin approach. There are two echelons, the first involves predicting the occurrence of lack-of-fusion porosity. The second echelon is aimed at the prediction of meltpool depth, grain size, and microhardness of samples in which no lack-of-fusion porosity was detected.

A supervised k-nearest neighborhood (kNN) machine learning model is employed at both hierarchical levels. A kNN model is selected owing to its simplicity, and its applicability to both classification and regression problems prevalent in the first and second echelons, respectively [97]. While more complex machine learning models, such as artificial neural networks were assessed, the results were only marginally better than kNN. On the other hand, the performance of simpler polynomial and logistic regression models deteriorated precipitously for prediction of grain size and microhardness.

### 4.3.2 Model Inputs, Training, and Testing.

To test the digital twin hypothesis, the prediction accuracy is assessed for four combinations of inputs to the kNN model: (i) processing parameters, power (P) and velocity (V); (ii) layer-wise mean and standard deviation of the sensor signatures, meltpool intensity ( $I_m$ ), end-of-cycle temperature ( $T_e$ ), and the interlayer time ( $t_1$ ); (iii), layer-wise mean and standard deviation of the two thermal simulation-derived quantifiers end-of-cycle temperature ( $\hat{T}_e$ ) and cooling time ( $\hat{t}_e$ ); and (iv) the digital twin model combining both the sensor signatures and simulation-derived quantifiers. Depending on the complexity of the task, between four and eight features are used in the digital twin. The classification results are reported in terms of the  $F_1$ -score and the regression accuracy is quantified with the  $R^2$ -adjusted measure [98]. These accuracy metrics are reported only for the testing data.

In this work, all sensor signatures were extracted on a layer-by-layer basis for each part as previously discussed in Sec. 4.1. The thermal history quantifiers, discussed in Sec. 4.2 and summarized in Figure 22, were extracted from the model based on a super-layer basis. Three actual layers were agglomerated into a super-layer. These model-derived quantifiers were assigned to each of the three agglomerated actual layers and spatially aligned to the corresponding sensor data.

Towards the prediction of part quality metrics, the measured porosity, meltpool depth, grain size, and microhardness must also be spatially aligned and aggregated on a layer-by-layer basis for each part. These are detailed below:

## (a) Porosity

Lack-of-fusion porosity was spatially aligned on a layer-by-layer basis to the as-printed part by measuring the distance from the top surface. In other words, we ascertain the distance of each

layer which contained lack-of-fusion porosity to the as-processed surface. The sensor signatures, thermal history quantifiers, and part quality metric (porosity) are thus spatially aligned on a layer-by-layer basis for machine learning training and testing.

# (b) Meltpool Depth

Meltpool depth  $(d_p)$  is measured only at the topmost as-processed surface of each sample in accordance with NASA MSFC-SPEC-3717 standard [48]. Consequently, only the top 10 actual layers of sensor signatures and thermal history quantifiers were used to predict the average meltpool depth for each sample. Thus the top 10 layers of sensor signatures and thermal history quantifiers are accorded the same measured meltpool depth  $(d_p)$ .

## (c) Grain Size & Microhardness

Both grain size and microhardness measurements, visualized in Figure 10, were spatially aligned on a layer-by-layer basis using the same methodology. For each part, all grain size and microhardness measurements taken at the same z-height were averaged. The surrounding approximately 125 layers were assigned the averaged grain size ( $\lambda_1$ ) and microhardness (Hv) measurements taken. These  $\lambda_1$  and Hv measurements are aligned to their corresponding sensor data and thermal history quantifiers.

Thus, the model learns the inherent variation in sensor signatures and thermal history quantifiers that generate meltpool depth  $(d_p)$ , grain size  $(\lambda_l)$ , and microhardness (Hv). For model training and testing, a conservative 60-40 split is used; 60% of the data is randomly selected for model training and 40% for testing. The train-test procedure is repeated 10 times to mitigate bias (10-fold cross-validation).

#### 5 Results

### 5.1 Porosity

As first noted in the context of Figure 7, lack-of-fusion porosity was observed when the laser power  $P \le 185$  W, viz., ~20% below the nominal laser power P = 230 W. This occurrence of lack-of-fusion porosity is further examined in Figure 23 in the context of the vase-shaped parts VS-N and VS-NP<sub>2</sub>. VS-N was processed under constant nominal laser power condition. For VS-NP<sub>2</sub> the laser power was reduced from the nominal to  $P_2 = 185$  W at a height of 16 mm (533 layers). Shown in Figure 23 are visualizations of the meltpool intensity ( $I_m$ ) and end-of-cycle temperature ( $T_e$ ) measured from the optical tomography and thermal sensors, respectively; the end-of-cycle temperature ( $T_e$ ) from the thermal simulation; and the optical micrographs at two representative locations on each sample.

In Figure 23, the occurrence of lack-of-fusion porosity in VS-NP<sub>2</sub> corresponds to regions of reduced meltpool intensity ( $I_m$ ), which in turn is correlated to the locations where laser power was reduced from nominal level of 230 W to 185 W at 16 mm build height. However, the occurrence of lack-of-fusion porosity is not visually apparent from either the end-of-cycle temperature ( $T_e$ ) measurements obtained from the thermal camera, nor in the predicted thermal simulations ( $\widehat{T}_e$ ).

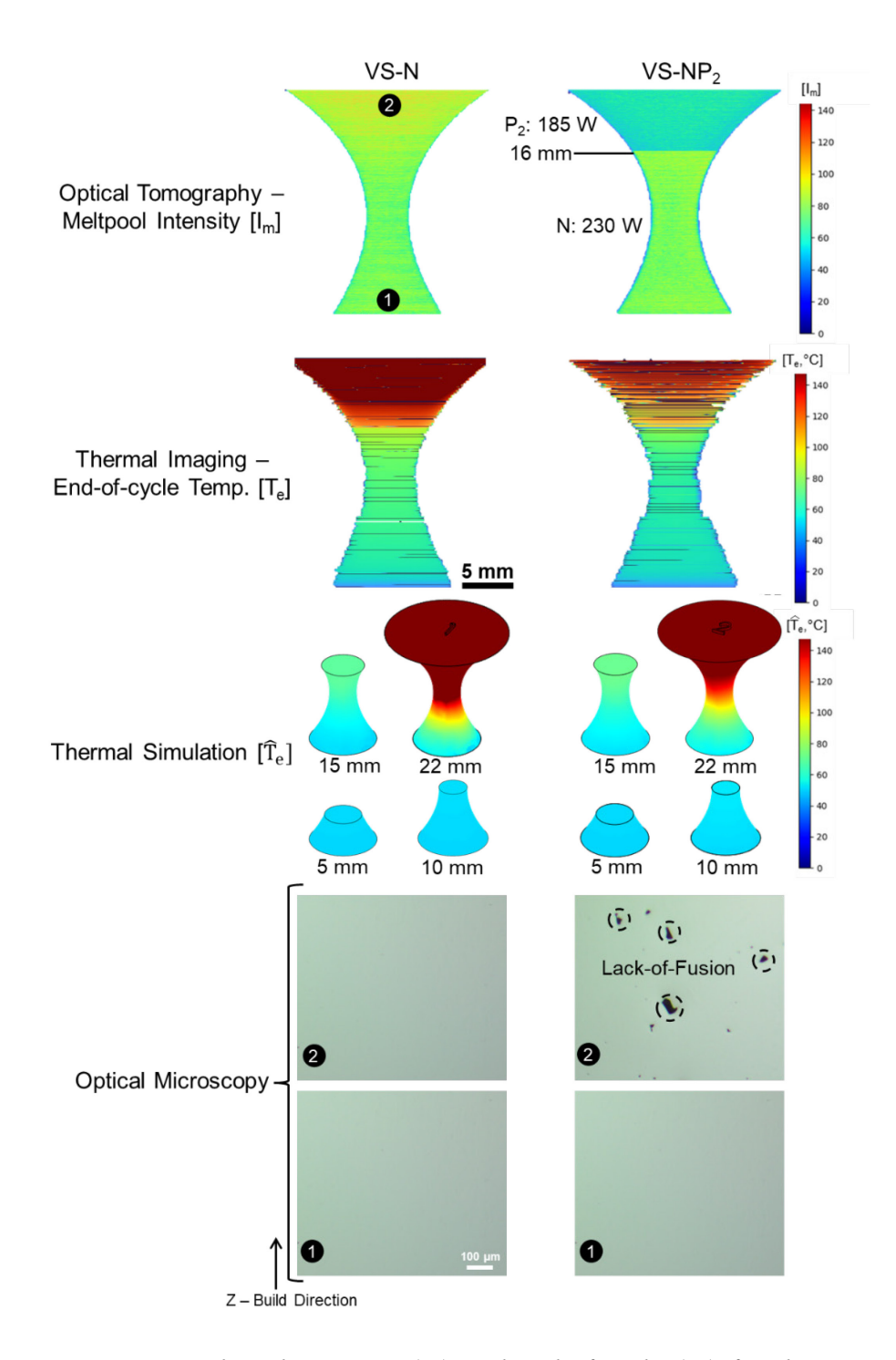


Figure 23: Representative meltpool intensity ( $I_m$ ) and end-of-cycle ( $T_e$ ) for the two solid vase shaped parts VS-N and VS-NP<sub>2</sub>; simulation of thermal history using the graph theory model; and optical microscopy at two locations. Lack-of-fusion porosity was observed at locations of VS-NP<sub>2</sub> when the laser power was reduced from 230 W to 185 W at 16 mm of build height.

Continuing with the analysis, in Figure 24 the occurrence of lack-of-fusion porosity is correlated to meltpool intensity ( $I_m$ ) from the optical tomography camera and the cooling time ( $\hat{t}_c$ ) derived from the thermal model. In Figure 24(a) the mean meltpool intensity ( $I_m$ ) over a layer for each part is plotted for the pore (red) and pore-free (blue) conditions. A clear segregation in the data is evident; lack-of-fusion porosity typically occurs when  $I_m < 50$  units. Similarly, in Figure 24(b), lack-of-fusion porosity is stratified with respect to the simulation-derived cooling time ( $\hat{t}_c$ ). The occurrence of lack-of-fusion porosity is exacerbated when  $\hat{t}_c \le 0.3$  s. This is to be expected as lack-of-fusion porosity results from insufficient input energy, which in turn is correlated with reduced meltpool intensity ( $I_m$ ), and rapid dissipation of heat, i.e., shorter duration of  $\hat{t}_c$ .

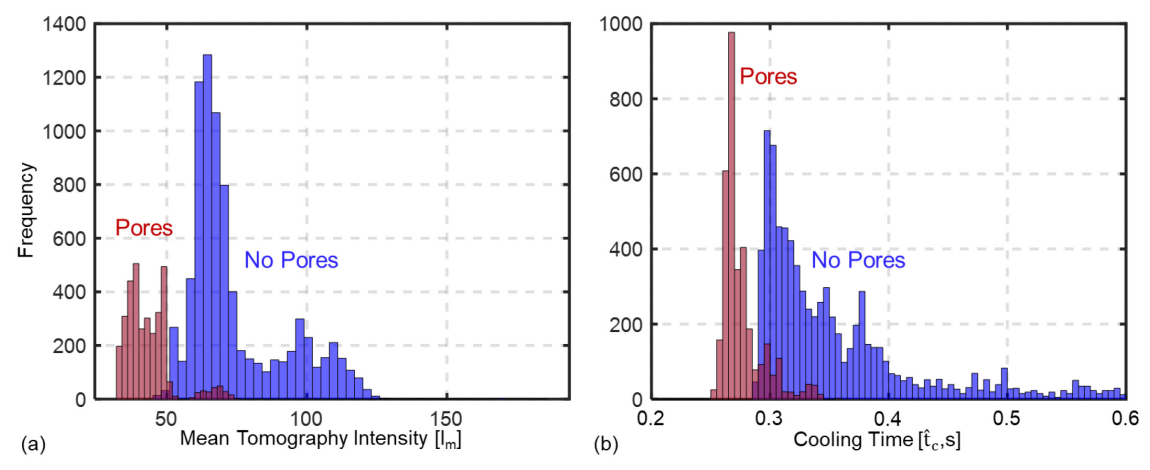


Figure 24: Histogram comparing the areas with no pores (blue) with pores (red) for all 18 parts analyzed in this work (n = 11,466). (a) Lack-of-fusion porosity is observed when meltpool intensity  $I_m < 50$  units (optical tomography). Likewise, lack-of-fusion porosity occurs when  $\hat{t}_c < 0.3$  s (thermal simulation).

Four features are used as inputs to the digital twin kNN model: (i) the mean meltpool intensity  $(I_m)$ , (ii) mean of end-of-cycle temperature  $(T_e)$  observed from the thermal camera, (iii) mean of end-of-cycle temperature  $(\widehat{T}_e)$  from the physics-based model, and (iv) mean of cooling time  $(\widehat{t}_c)$ . The model is trained to classify the part quality into lack-of-fusion porosity vs. no porosity, viz., a two-class problem. The kNN model utilized 11,466 data points with a conservative 60-40 train-

test split. To explain further, 60% of the data (6,880 data points) were randomly selected for training. The remaining 40% of the data (4,586 data points) were used for testing the model. This randomized train-test split was performed 10 times to ensure that the model did not fit on a favorable selection of data points (10-fold cross-validation).

The testing results are reported in Table 3. First, when using only the processing parameters of laser power (P) and scan velocity (V), the model detected lack-of-fusion porosity on a layer-by-layer basis with an F<sub>1</sub>-score of 96.6% (std. dev. of 10-fold cross-validation,  $\sigma = 0.3\%$ ). This confirms that lack-of-fusion porosity is primarily parameter induced, as demarcated in Figure 7. When only the two sensor-based features are used, the presence of lack-of-fusion porosity is also detected with a statistical F<sub>1</sub>-score of 96.6% ( $\sigma = 0.3\%$ ), due to the high correlation between input energy density (E<sub>v</sub>) and the mean meltpool intensity (I<sub>m</sub>). Next, when only the two quantifiers from the thermal model, i.e.,  $\widehat{T}_e$  and  $\widehat{t}_e$ , were used as inputs to the kNN, the prediction fidelity increased to F<sub>1</sub>-score  $\sim$  98.5% ( $\sigma = 0.4\%$ ). Finally, when the digital twin is implemented, where both sensor signatures and thermal history quantifiers (total of 4 features) are used as inputs to the kNN model, the F<sub>1</sub>-score improves to 99.3% ( $\sigma = 0.1\%$ ). *Additionally, the digital twin model resulted in a false positive rate*  $\alpha = 0.5\%$  and a false negative rate,  $\beta = 0.04\%$ . The low standard deviation over the 10 train-test cycles indicates that the model results are repeatable and not stochastic.

Table 3: kNN results for the binary prediction of lack-of-fusion porosity as a function of different inputs. The model fidelity is quantified in terms of the  $F_1$ -score with 10-fold cross-validation standard deviation reported in parenthesis. Testing data (n = 4,586 data points) is reported.

Data Source	Predictors (Model Inputs)	F <sub>1</sub> -Score
Processing	• Laser power (P)	96.6% (0.3%)
Parameters	• Laser Velocity (V)	
Sensor Signatures	Mean Meltpool Intensity [I <sub>m</sub> ]	96.6% (0.3%)
(A)	• Mean end-of-cycle Temperature [Te,°C]	` ′
Thermal History	• Mean end-of-cycle Temperature $[\hat{T}_e, {}^{\circ}C]$	98.5% (0.4%)
Quantifiers (B)	<ul> <li>Mean Cooling Time [t̂c,s]</li> </ul>	70.570 (0.170)
(A+B) Digital	Use both sensor and model features (4 features)	99.3% (0.1%)
Twin	Ose both sensor and model leatures (4 leatures)	77.5 /0 (0.1 /0)

# 5.2 Meltpool Depth

The meltpool depth  $(d_p)$  was measured based on NASA MSFC-SPEC-3717 standard [48]. In Figure 25, the meltpool depth  $(d_p)$  is plotted as a function of the energy density  $(E_v)$  for 10 samples without lack-of-fusion porosity. The data are stratified as under penetration  $(d_p \le 60 \ \mu m, \le 2 \ layers)$ , nominal penetration  $(60 \ \mu m < d_p \le 90 \ \mu m, 2-3 \ layers)$ , and over penetration  $(d_p > 90 \ um, > 3 \ layers)$ . Under nominal parameters with  $E_v = 71 \ J \cdot mm^{-3}$ , the measured meltpool depth is  $\sim 70 \ \mu m$  which is between the desired 2-3 layers of meltpool penetration. Noting that the layer height  $L = 30 \ \mu m$ . In Figure 25 the average meltpool depth  $(d_p)$  increases proportionally with  $E_v$ , however, the trend is not linear.

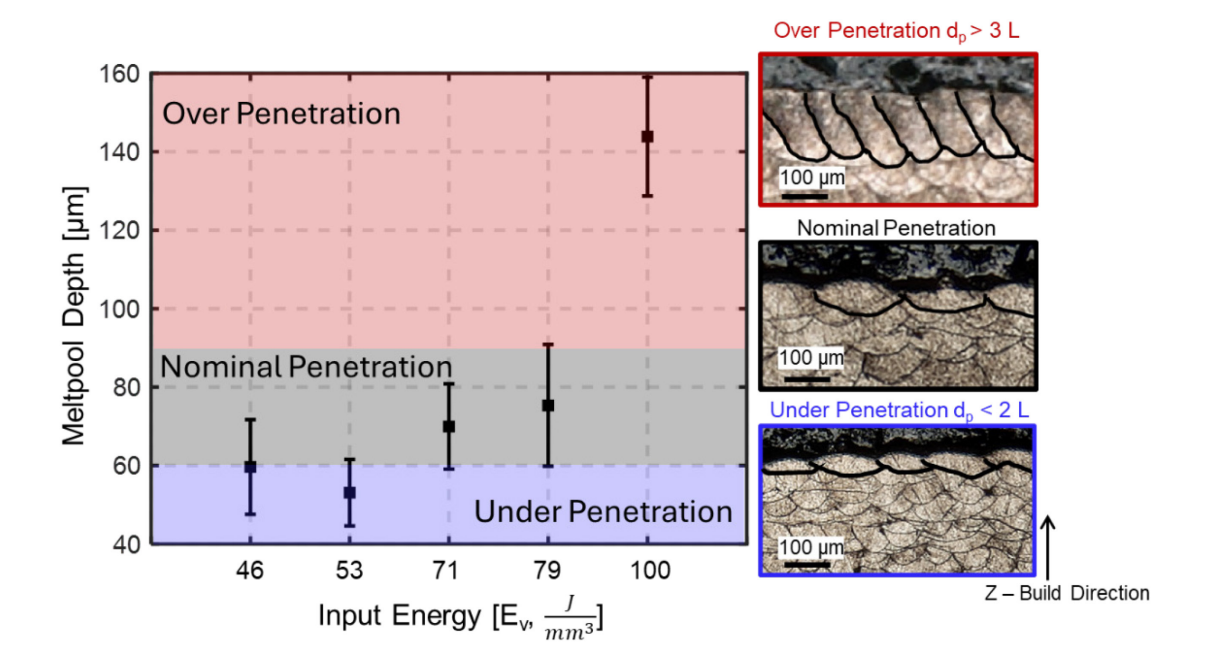


Figure 25: The effect of energy density  $(E_v)$  on meltpool depth  $(d_p)$  for all parts. Three clusters were segmented in this work. Note the nonlinear trend between input energy and meltpool depth.

Figure 26 compares the meltpool intensity ( $I_m$ ), end-of-cycle temperature ( $T_e$ ), and thermal simulation for two of the psi-shaped geometries,  $\Psi$ -N and  $\Psi$ -E<sub>4</sub>. Also shown in Figure 26 are the corresponding optical micrographs depicting the meltpool boundaries at the top layers. For  $\Psi$ -N  $d_p$  = 73.5  $\mu$ m, viz., 2.5 layers deep; in the case of  $\Psi$ -E<sub>4</sub>,  $d_p$   $\approx$  144  $\mu$ m, viz., 4.8 layers deep indicating

over-penetration. In Figure 26, the meltpool depth  $(d_p)$  is correlated positively to  $I_m$  and  $T_e$ . A positive correlation is also visually evident between  $d_p$  and simulation-derived  $\widehat{T}_e$ .

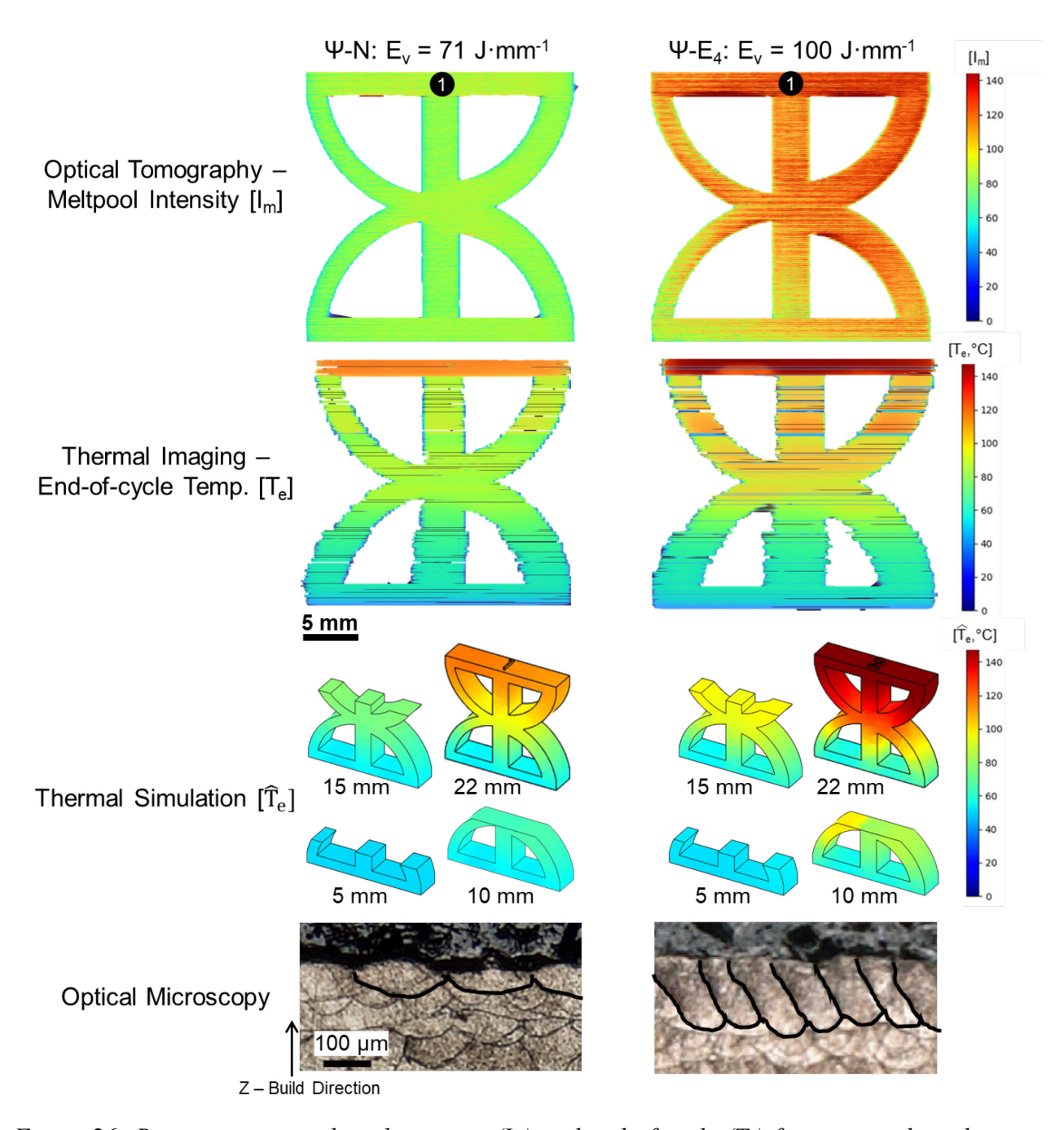


Figure 26: Representative meltpool intensity  $(I_m)$  and end-of-cycle  $(T_e)$  for two psi shaped parts  $\Psi$ -N and  $\Psi$ -E<sub>4</sub>; simulation of thermal history using the graph theory model; and optical microscopy at the top surface. The meltpool depth  $(d_p)$  was observed to be significantly deeper in  $\Psi$ -E<sub>4</sub> than  $\Psi$ -N due to increased thermal input energy and heat retention.

Visualized in Figure 27(a) and (b), respectively, is the correlation of the measured meltpool depth ( $d_p$ ) with the sensor-based signature meltpool intensity ( $I_m$ ), and the model-predicted cooling time ( $\hat{t}_c$ ). Figure 27 confirms that  $I_m$  and  $\hat{t}_c$  are positively correlated to  $d_p$ , confirming that deeper solidified meltpools are symptomatic of increased heat retention. Further, Figure 27 reveals that  $I_m$  and  $\hat{t}_c$  are capable of distinguishing between under penetration ( $d_p \le 60~\mu m$ ,  $\le 2$  layers), nominal penetration ( $60~\mu m < d_p < 90~\mu m$ , 2-3 layers), and over penetration ( $d_p > 90~\mu m$ , > 3 layers). In Figure 27 sensor signatures and model quantifiers for only the top 10 layers from the 10 samples without lack-of-fusion porosity are used, corresponding to 100 measurements of meltpool depth ( $d_p$ ).

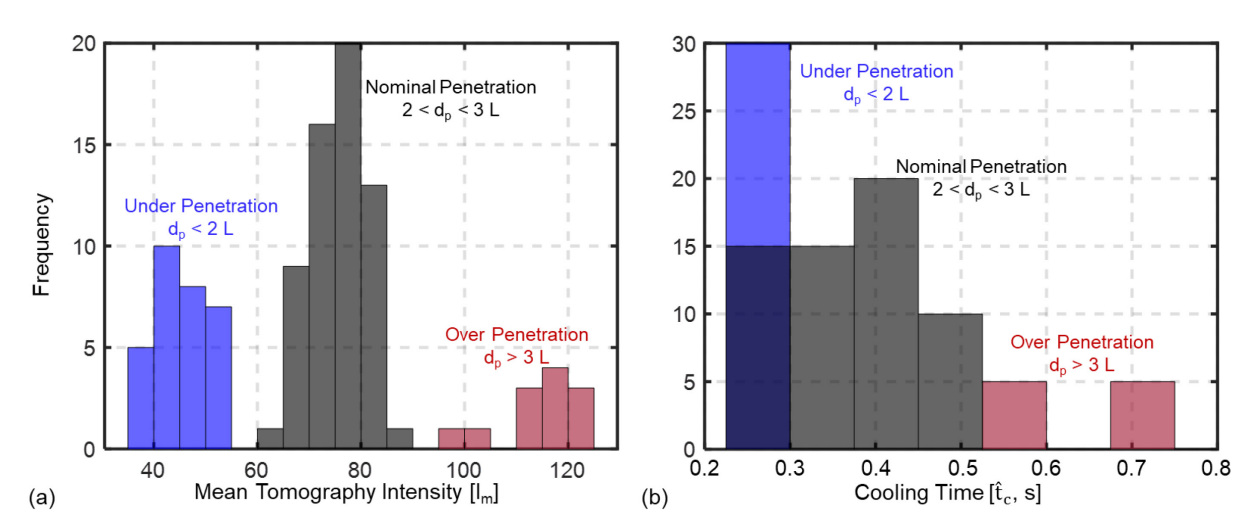


Figure 27: Histogram of the meltpool depth  $(d_p)$  as a function of the (a) meltpool intensity  $(I_m)$ , and (b) cooling time  $(\hat{t}_c)$  (n = 100). The meltpool depth  $(d_p)$  is proportional to both  $I_m$  and  $\hat{t}_c$ .

To predict meltpool depth  $(d_p)$ , four features, namely, the mean meltpool intensity  $(I_m)$ , and mean of end-of-cycle  $(T_e)$  from the thermal camera, end-of-cycle temperature  $(\widehat{T}_e)$ , and cooling time  $(\widehat{t}_c)$  are used in a regression kNN machine learning model. These same four features were also used for the prediction of porosity in Sec. 5.1. The model uses 100 data points with a 60-40 traintest split, in which 60% of the data points were randomly selected for training the regression model and the remaining 40% of the data was used for testing *the developed regression model to predict* 

the specific meltpool depth at the top surface of each part. The randomized train-test split was performed 10-fold to mitigate overfitting (10-fold cross-validation).

As depicted in Table 4, when using only the processing parameters of laser power (P) and scan velocity (V), the model accurately predicted the meltpool depth with an R²-adj of 98.1% (std. dev. over 10-fold cross-validation  $\sigma=0.8\%$ ). This indicates that meltpool depth is primarily dependent on the input energy from the laser. When the two sensor-based features are used, the meltpool depth is predicted with an increased fidelity R²-adj  $\sim$  99.3%. When only the thermal history quantifiers are used as inputs the prediction accuracy of meltpool depth remains consistent at R²-adj  $\sim$  99.3%, albeit model uncertainty increases to  $\sigma=2.3\%$  from  $\sigma=1.7\%$ . Finally, when both the thermal history quantifiers and sensor signatures are used as inputs, the prediction accuracy improves marginally to R²-adj  $\sim$  99.6% with a mean squared error (MSE) of  $\sim$ 1  $\mu$ m. The relatively high prediction accuracy is on account of the positive correlation between the sensor signatures, thermal history quantifiers, and different levels of meltpool depth (dp) as shown in Figure 27.

Table 4: kNN results for the regression prediction of meltpool depth as a function of different inputs. The model fidelity is quantified in terms of  $R^2$ -adj. with 10-fold cross-validation standard deviation reported in parenthesis.

Data Source	Predictors (Model Inputs)	$R^2$ -adj.
Processing Parameters	<ul><li>Power (P)</li><li>Velocity (V)</li></ul>	98.1% (0.8%)
Sensor Signatures (A)	<ul> <li>Mean Meltpool Intensity [I<sub>m</sub>]</li> <li>Mean EOC Temperature [T<sub>e</sub>,°C]</li> </ul>	99.3% (1.7%)
Thermal History Quantifiers (B)	<ul> <li>Mean EOC Temperature [Îe,°C]</li> <li>Mean Cooling Time [îe,s]</li> </ul>	99.3% (2.3%)
(A+B) Digital Twin	Use both sensor and model features (4 features)	99.6% (1.0%)

## 5.3 Grain Size

Plotted in Figure 28 is the grain size, in terms of the primary dendritic arm spacing (PDAS,  $\lambda_1$ ), as a function of the energy density (E<sub>v</sub>) for 10 of the 18 parts without lack-of-fusion porosity. The grain size measurements are stratified into three levels for visualization purposes. The three levels are: small grains,  $\lambda_1 \leq 550$  nm; medium grains, 550 nm  $< \lambda_1 \leq 600$  nm; and large grains  $\lambda_1 > 600$  nm. As the energy density (E<sub>v</sub>) is increased beyond the nominal conditions of E<sub>v</sub> = 71 J·mm<sup>-3</sup>,  $\lambda_1$  also increases on account of grain coarsening. To explain further, as E<sub>v</sub> increases, heat retention increases, and the cooling rate decreases, which provides the dendrites more time to grow (grain coarsening) [99]. However, the trend between  $\lambda_1$  vs. E<sub>v</sub> is nonlinear due to the complex effect of part shape.

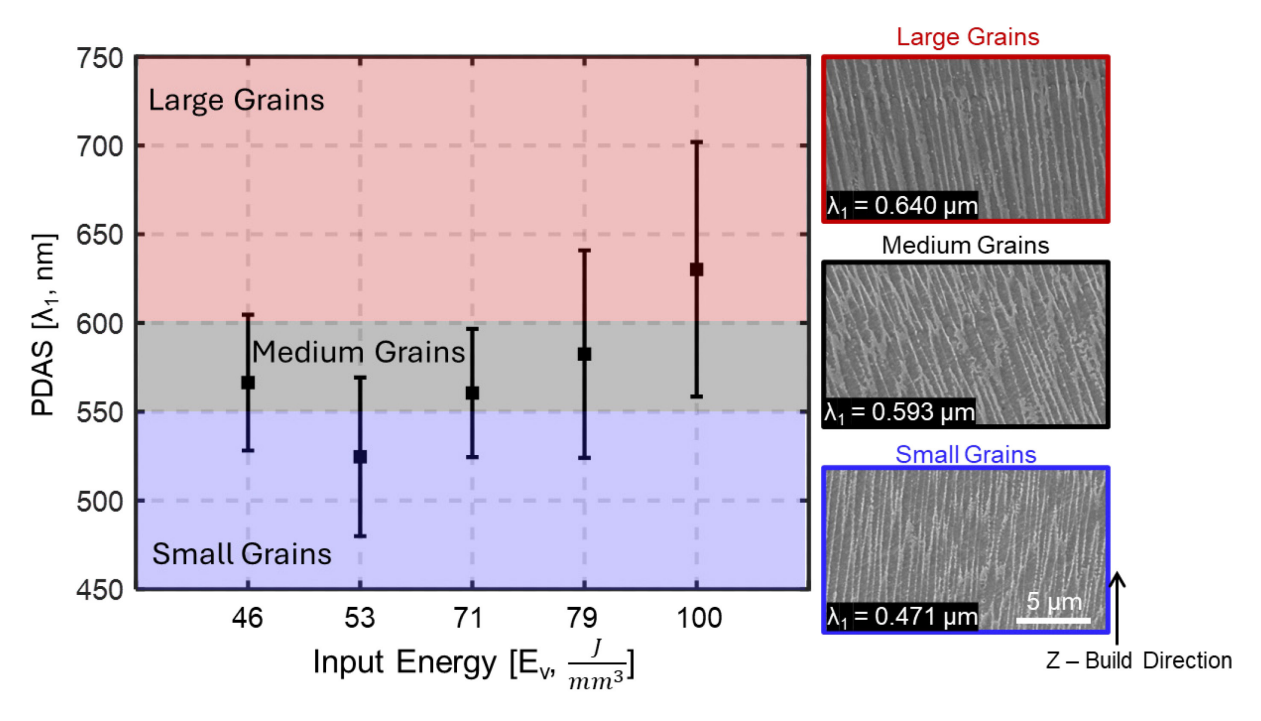


Figure 28: The effect of energy density  $(E_v)$  on primary dendritic arm spacing  $(\lambda_l)$  for all 10 parts without porosity. Three clusters are observed in the data. An increasing, albeit nonlinear, trend in  $\lambda_l$  vs. Ev is discerned, indicating that heat retention results in grain coarsening.

This grain coarsening effect is visualized in Figure 29 for three overhang geometries (O-N, O-E<sub>3</sub>, and O-E<sub>4</sub>) with progressively increasing energy density. Figure 29 depicts the meltpool intensity (I<sub>m</sub>) from optical tomography and end-of-cycle infrared images (T<sub>e</sub>), the thermal simulation results, and representative SEM images. The increase in energy density manifests in higher meltpool intensity I<sub>m</sub> and T<sub>e</sub>, and heat retention in the overhang section, which leads to increase in the grain size ( $\lambda_1$ ). For example, O-N at the demarcated location, viz. layer ~600 (~18 mm),  $\lambda_1 = 471$  nm. A similar location on O-E<sub>3</sub> the  $\lambda_1 = 593$  nm, and for O-E<sub>4</sub>  $\lambda_1 = 640$  nm.

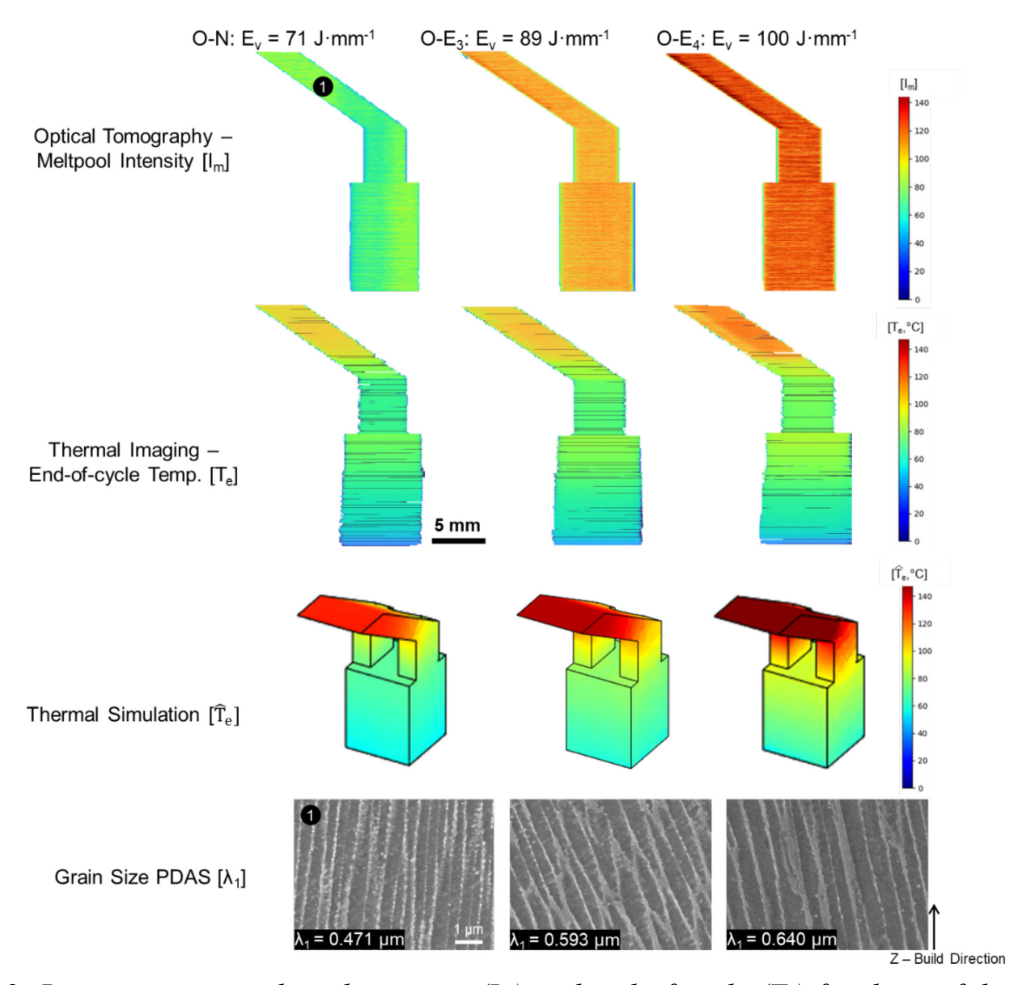


Figure 29: Representative meltpool intensity ( $I_m$ ) and end-of-cycle ( $T_e$ ) for three of the overhang shaped parts O-N, O-Ev<sub>3</sub>, and O-Ev<sub>4</sub>; simulation of thermal history using the graph theory model; and SEM images in the overhang region. The grain size ( $\lambda_1$ ) increased proportional to the input energy and heat retention.

In Figure 30, the distribution of the meltpool intensity ( $I_m$ ) and model-predicted cooling time ( $\hat{t}_c$ ) are stratified for the three levels of primary dendritic arm spacing ( $\lambda_1$ ). This stratification is done only for visualization purposes. The data in Figure 30 encompasses 5,271 data points. These histograms confirm the general trend that an increase in  $I_m$  and  $\hat{t}_c$  is correlated positively with  $\lambda_1$ . However, there is significant overlap between the three classes. Therefore, prediction of  $\lambda_1$  is considerably more challenging than prediction of lack-of-fusion porosity and meltpool depth.

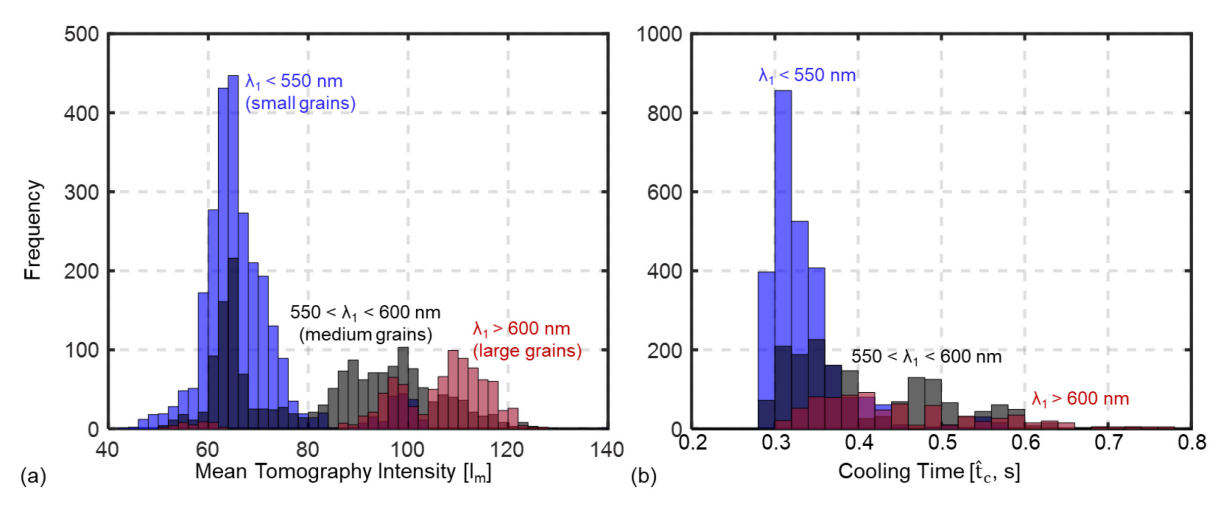


Figure 30: Histogram of grain size  $(\lambda_l)$  as a function of the (a) meltpool intensity  $(I_m)$ , and (b) cooling time  $(\hat{t}_c)$  estimated from the thermal model (n = 5,271). The grain size is generally proportion to  $I_m$  and  $\hat{t}_c$ , albeit there is considerable overlap.

Next, a kNN is trained to predict the *specific grain size value*  $\lambda_1$  *on a layer-by-layer basis*, as a function of processing parameters, sensor signatures, and thermal history quantifiers as listed in Table 5. These kNN regression models used 5,271 data points (layers). A 60-40 train-test split is implemented, in which 60% of the data points were randomly selected for training the regression model and the remaining 40% of the data was used for testing the model. This randomized traintest cycle was iterated 10-fold. As depicted in Table 5, using the processing parameters,  $\lambda_1$  is predicted with R<sup>2</sup>-adj.  $\sim$  44% ( $\sigma$  = 1.8%). Thus, grain size is not predicted with appreciable accuracy as a function of processing parameters alone.

When the three sensor-based signatures indicated in Table 5 are used as inputs,  $\lambda_1$  is predicted with an R<sup>2</sup>-adj. ~ 85%. With just the two thermal history quantifiers as inputs the prediction accuracy decreases to R<sup>2</sup>-adj ~ 80%. Finally, when both sensor signatures and thermal history quantifiers (5 input features) are used, the prediction accuracy increases significantly to R<sup>2</sup>-adj. ~ 93% with a MSE of ~0.4 nm. Notably the prediction uncertainty, quantified in terms of the standard deviation ( $\sigma$ ) over the 10 cross-validation cycles, for the digital twin approach is significantly smaller ( $\sigma$  ~ 0.6%) compared to using either sensor signatures ( $\sigma$  ~ 1.3%) or thermal history quantifiers ( $\sigma$  ~ 1.9%) alone. Indeed, this result is in accordance with our previous work, where the two thermal history quantifiers were used for the prediction of grain size ( $\lambda_1$ ) in Inconel 718. The prediction accuracy in this previous work was ~ 80% [81].

Table 5: kNN regression results for the regression prediction of grain size (PDAS,  $\lambda_l$ ) as a function of different inputs. The model fidelity is quantified in terms of the  $R^2$ -adj. value with 10-fold cross-validation standard deviation reported in parenthesis.

Data Source	Predictors (Model Inputs)	R <sup>2</sup> -adj.
Processing	• Power (P)	43.9% (1.8%)
Parameters	<ul> <li>Scan Velocity (V)</li> </ul>	43.770 (1.070)
Sensor Signatures	• Mean Meltpool Intensity [I <sub>m</sub> ]	
	<ul> <li>Mean End-of-Cycle Temperature [T<sub>e</sub>, °C]</li> </ul>	85.7% (1.3%)
(A)	• Inter-Layer-Time [t <sub>l</sub> ,s]	
Thermal History	<ul> <li>Mean End-of-Cycle Temperature [Îe, °C]</li> </ul>	80.8% (1.9%)
Quantifiers (B)	<ul> <li>Mean Cooling Time [t̂c, s]</li> </ul>	00.070 (1.970)
(A+B) Digital	• Use both sensor and model features (5 features)	93.7% (0.6%)
Twin	• Use both sensor and model features (5 features)	75.1 /0 (0.0 /0)

### 5.4 Microhardness

In Figure 31, the microhardness (Hv) for 11 samples without lack-of-fusion porosity is plotted as a function of energy density ( $E_v$ ), summarizing 6,279 data points. The microhardness increases as the input energy ( $E_v$ ) increases. In Figure 31, the microhardness is stratified into two levels, *for visualization purposes*, with mean  $Hv_{0.3} \leq 320$  (low microhardness), and  $Hv_{0.3} > 320$  (high hardness). The large relative variation in the microhardness, even under nominal processing conditions of  $E_v = 71$  J·mm<sup>-3</sup>, indicates complex interaction of thermal history, metallurgical phenomena, and process stochasticity.

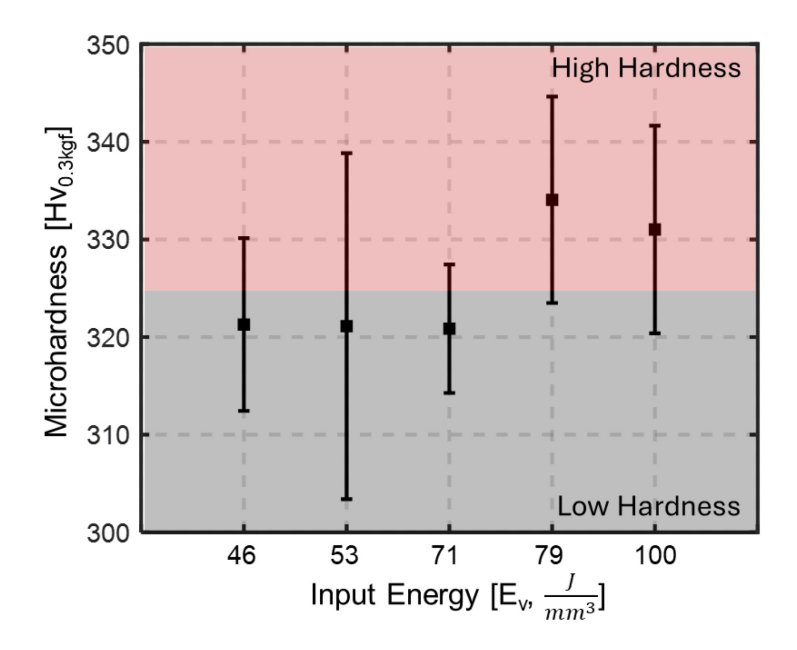


Figure 31: The effect of energy density  $(E_v)$  on microhardness (Hv) for all 10 parts without porosity. Two clusters are observed in the data at mean  $Hv \sim 320$  and  $Hv \sim 330$  (n = 6, 279)

Comparing Figure 28 and Figure 31 it is observed that both grain size ( $\lambda_1$ ) and microhardness (Hv) increase with increasing E<sub>v</sub>. However, microhardness (Hv) is typically inversely proportional to grain size ( $\lambda_1$ ) on account of the Hall-Petch effect [100]. A potential explanation for the counterintuitive trend of microhardness increasing with grain size is on account of the precipitation

hardening nature of Inconel 718. The increased heat retention and increased cooling time (reduced cooling rate) at elevated  $E_v$  is likely to facilitate the precipitation of nano-scale  $\gamma$ " Ni<sub>3</sub>Nb particles in Inconel 718 (precipitation hardening) [100-102]. The formation of  $\gamma$ " phases enhances microhardness and mechanical properties, such as yield strength. Investigating the cause of increase in microhardness with increase in  $E_v$  is beyond the scope of this work.

Figure 32 visualizes the optical tomography, infrared images, and thermal simulations for the two tower geometries, T-N and T-NP<sub>3</sub>P<sub>4</sub>. Additionally reported in Figure 32 are microhardness readings in the vicinity of the hexagon-shaped cavity. Unlike previous cases for porosity and meltpool depth, the difference in the sensor data and thermal simulation are not significant between the two parts, albeit the meltpool intensity (I<sub>m</sub>) responds to change in processing conditions in T-NP<sub>3</sub>P<sub>4</sub>. The subtle change in the thermal distribution affects the microhardness. The microhardness of the region around the cavity for T-N is markedly higher compared to T-NP<sub>3</sub>P<sub>4</sub>, however there tends to be a large variation in microhardness in sample T-N; with a range in microhardness greater-than 30 Hv<sub>0.3</sub> in comparison to a range of ~15 Hv<sub>0.3</sub> for sample T-NP<sub>3</sub>P<sub>4</sub>.

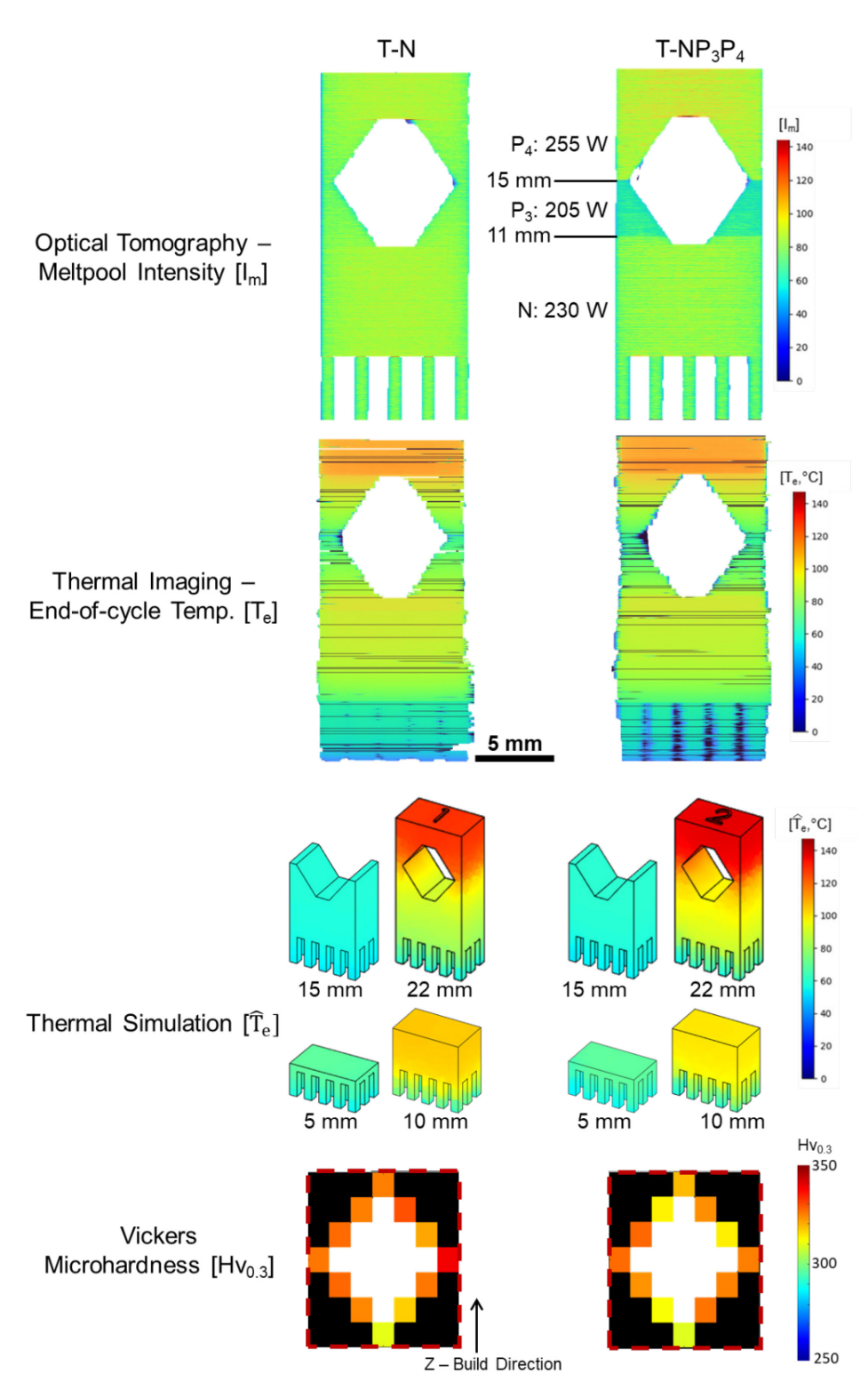


Figure 32: Representative meltpool intensity ( $I_m$ ) and end-of-cycle ( $T_e$ ) for the two tower-shaped geometries T-N and T- $NP_3P_4$ ; simulation of thermal history using the graph theory model; and microhardness readings near the hexagonal cavity. The microhardness is higher by 30 units for T-N, however the microhardness is generally higher.

Shown in Figure 33 are histograms comparing meltpool intensity obtained from the optical tomography camera ( $I_m$ ) and cooling time ( $\hat{t}_c$ ) from the thermal model for three levels of microhardness (Hv), encompassing 6,279 data points. *For visualization purposes*, the three levels of microhardness are: Hv < 300 (low); 300 < Hv < 325 (medium); and Hv > 325 (high). Unlike porosity and meltpool depth, there is significant overlap between the various levels of Hv found in this work. Consequently, compared to previous cases, the prediction of microhardness would require more input features to the kNN machine learning model.

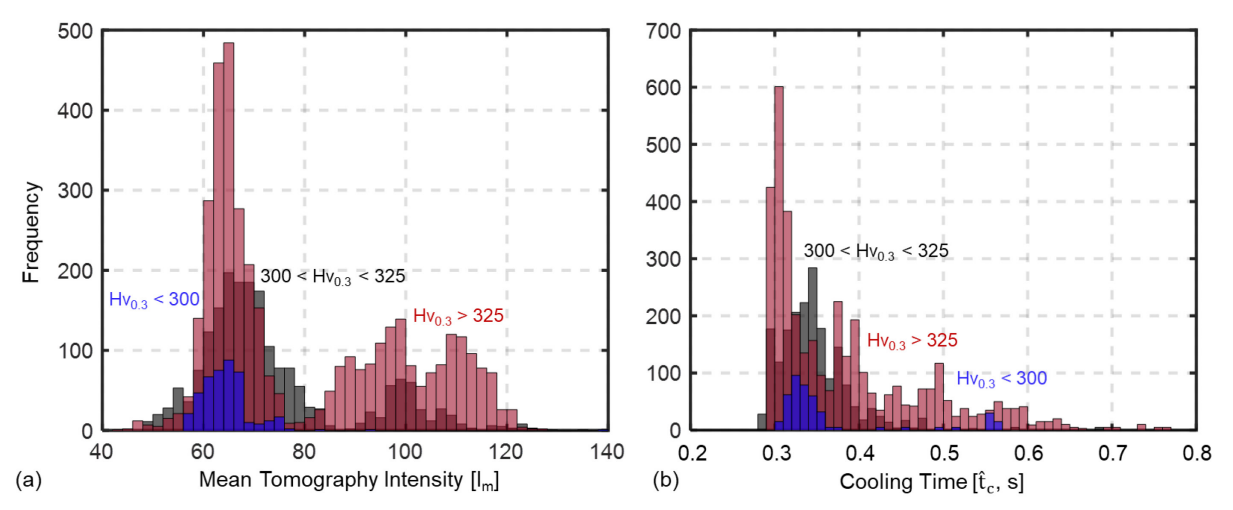


Figure 33: Histogram of the microhardness (Hv) as a function of (a) meltpool intensity ( $I_m$ ), and (b) cooling time ( $\hat{t}_c$ ) estimated from the thermal model (n = 6,279). The microhardness is proportional to  $I_m$  and  $\hat{t}_c$ , however the large variation in the data evades visual clustering.

The *specific microhardness value for each layer* is predicted using kNN regression models with processing parameters, sensor signatures, and thermal history quantifiers as inputs. The kNN models used 6,279 data points, with a 60-40 train-test split and 10-fold cross-validation. As shown in Table 6, using only processing parameters, laser power (P) and velocity (V), the microhardness was predicted with accuracy R<sup>2</sup>-adj ~7.5%. Thus, confirming that the variation in microhardness cannot be predicted as a function of parameters. When the sensor signatures were used as inputs, the microhardness is predicted with an R<sup>2</sup>-adj. ~ 84%. Using the thermal history quantifiers, the

prediction accuracy improves to  $R^2$ -adj. ~ 85%. When both in-situ sensor data and sensor signatures are used together in a digital twin model (8 input features), the accuracy increases significantly to  $R^2$ -adj ~ 91% with a MSE of ~0.62 Hv<sub>0.3</sub>.

Table 6: kNN results for the regression prediction of microhardness as a function of different inputs. The model fidelity is quantified in terms of the  $R^2$ -adj. value with 10-fold cross-validation standard deviation reported in parenthesis.

Data Source	Predictors (Model Inputs)	$R^2$ -adj.
Process Parameters	<ul><li>Power (P)</li><li>Scan Velocity (V)</li></ul>	7.5% (2.3%)
Sensor Signatures (A)	<ul> <li>Mean Meltpool Intensity [I<sub>m</sub>]</li> <li>Std. Dev. Meltpool Intensity [σI<sub>m</sub>]</li> <li>Mean End-of-Cycle Temperature [T<sub>e</sub>,°C]</li> <li>Std. Dev. End-of-Cycle Temperature [σT<sub>e</sub>,°C]</li> <li>Inter-Layer-Time [t<sub>l</sub>,s]</li> </ul>	84.0% (2.3%)
Thermal History Quantifiers (B)	<ul> <li>Mean End-of-Cycle Temperature [T̂<sub>e</sub>,°C]</li> <li>Std. Dev. End-of-Cycle Temperature [σT̂<sub>e</sub>,°C]</li> <li>Mean Cooling Time [t̂<sub>c</sub>, s]</li> </ul>	85.4% (1.8%)
(A+B) Digital Twin	Use both sensor and model features (8 features)	91.1% (1.6%)

### **6** Conclusions and Future Work

Qualification of LPBF part quality is presently dependent on expensive and time-intensive post-process characterization using X-ray CT and metallographic analysis. To accelerate part qualification, this work developed a digital twin strategy that combined in-situ heterogeneous sensor data and computational thermal modeling within machine learning. The approach was applied for predicting lack-of-fusion porosity, meltpool depth  $(d_p)$ , grain size  $(\lambda_1)$ , and microhardness (Hv) in Inconel 718 parts across a range of processing parameters and part shapes. The approach predicted the foregoing part quality aspects with statistical fidelity exceeding 90%.

Specific outcomes are as follows:

(1) In-situ data from an optical tomography and a long wavelength infrared imaging camera was captured during the LPBF of Inconel 718 samples encompassing 18 different part shapes and processing conditions. From this data instantaneous meltpool intensity and

- end-of-cycle temperature were extracted. These sensor signatures capture complementary aspects of the process. In parallel, a mesh-free physics-based thermal computational modeling approach was used to predict consequential aspects of the thermal history, such as the end-of-cycle temperature and cooling time. The model was validated with in-situ experimental thermal imaging data.
- (2) Signatures acquired from the in-situ sensor data, and quantifiers of the thermal history from the physics-based model were used as inputs into a K-nearest neighbors (kNN) machine learning algorithm. The ground truth for the kNN was obtained from metallographic characterization. The kNN was trained to detect lack-of-fusion porosity with a fidelity exceeding 99% (F<sub>1</sub>-score), meltpool depth (d<sub>p</sub>) with R<sup>2</sup>-adj.  $\sim$  99%, grain size in terms ( $\lambda_1$ ) with R<sup>2</sup>-adj.  $\sim$  93%, and microhardness (Hv) R<sup>2</sup>-adj.  $\sim$  91%.
- (3) The prediction accuracy of the digital twin approach was superior to either using only sensor-based or thermal history quantifiers as inputs to the kNN model. For example, the digital twin approach predicted grain size ( $\lambda_1$ ) with accuracy R<sup>2</sup>-adj. ~ 93%, compared to R<sup>2</sup>-adj. ~ 85% and R<sup>2</sup>-adj. ~ 80%, respectively, when only sensor-based and thermal history quantifiers were used.
- (4) The occurrence of lack-of-fusion porosity and meltpool depth were predicted as function of process parameters, namely, laser power and velocity with statistical fidelity exceeding 95%. However, process parameters would not account for the effect stochastic errors, such as disruption of gas flow and variation in the deposition of height of the powder, that can greatly affect the porosity formation and meltpool depth. Therefore, it is pertinent and advantageous to perform in-situ monitoring for detection of porosity and meltpool depth to ascertain that the printing process is stable and performing as expected.

This work takes an important first step towards realizing an in-situ *Born Qualified* quality assurance paradigm in LPBF. In addition to the ability to predict coarse level grain size ( $\lambda_1$ ) and microhardness (Hv) on a layer-by-layer basis, the developed approach is capable of monitoring process stability. Thus, ensuring that no lack-of-fusion porosity is being developed and that the meltpool depth ( $d_p$ ) is within nominal parameters. If either of these values vary from the set nominal, from processing parameters, machine operators can know that there is a systemic problem with the machine such as improper gas flow.

Remark on transferability of the proposed digital twin approach: In our previously published work, we have used the same machine, material (Inconel 718), and sensing setup under similar operating conditions as those described in this paper to detect a variety of flaw formation ranging from porosity, distortion, recoater interactions, and scan path errors [26]. Indeed, the cone and overhang geometries described herein was also examined in our prior work. In the prior work described in Ref. [26] we showed that there was negligible difference in sensor signatures acquired across four different build plates with identical parts. This lack of variability of build plates was ensured through calibration of optical tomography and infrared thermal imaging to the specific material and ambient process conditions. Given the demonstrated robustness of the sensors used for monitoring the process, and that thermal model accounts for the effect of part shape, processing conditions, materials properties and build orientation, it would be reasonable to surmise that the digital twin approach would be transferable across build plates. Nevertheless, in our future work we will endeavor to ascertain transferability across different build plates. Lastly, we are exploring approaches to improve the resolution of the model to predict other microstructural characteristics, such as grain orientation and texture.

#### References

- [1] A. Keshavarzkermani, E. Marzbanrad, R. Esmaeilizadeh, Y. Mahmoodkhani, U. Ali, P.D. Enrique, N.Y. Zhou, A. Bonakdar, E. Toyserkani, An investigation into the effect of process parameters on melt pool geometry, cell spacing, and grain refinement during laser powder bed fusion, Optics & Laser Technology 116 (2019) 83-91.
- [2] A. Marques, Â. Cunha, M.R. Silva, M.I. Osendi, F.S. Silva, Ó. Carvalho, F. Bartolomeu, Inconel 718 produced by laser powder bed fusion: an overview of the influence of processing parameters on microstructural and mechanical properties, The International Journal of Advanced Manufacturing Technology 121(9) (2022) 5651-5675.
- [3] S. Sanchez, P. Smith, Z. Xu, G. Gaspard, C.J. Hyde, W.W. Wits, I.A. Ashcroft, H. Chen, A.T. Clare, Powder Bed Fusion of nickel-based superalloys: A review, International Journal of Machine Tools and Manufacture 165 (2021) 103729.
- [4] W.J. Sames, F.A. List, S. Pannala, R.R. Dehoff, S.S. Babu, The metallurgy and processing science of metal additive manufacturing, International Materials Reviews 61(5) (2016) 315-360.
- [5] T. DebRoy, H.L. Wei, J.S. Zuback, T. Mukherjee, J.W. Elmer, J.O. Milewski, A.M. Beese, A. Wilson-Heid, A. De, W. Zhang, Additive manufacturing of metallic components Process, structure and properties, Progress in Materials Science 92 (2018) 112-224.
- [6] B. Blakey-Milner, P. Gradl, G. Snedden, M. Brooks, J. Pitot, E. Lopez, M. Leary, F. Berto, A. du Plessis, Metal additive manufacturing in aerospace: A review, Materials & Design 209 (2021) 110008.
- [7] G.R. Kumar, M. Sathishkumar, M. Vignesh, M. Manikandan, G. Rajyalakshmi, R. Ramanujam, N. Arivazhagan, Metal additive manufacturing of commercial aerospace components A comprehensive review, Proceedings of the Institution of Mechanical Engineers, Part E: Journal of Process Mechanical Engineering (2022) 09544089221104070.
- [8] A. Mostafaei, C. Zhao, Y. He, S. Reza Ghiaasiaan, B. Shi, S. Shao, N. Shamsaei, Z. Wu, N. Kouraytem, T. Sun, J. Pauza, J.V. Gordon, B. Webler, N.D. Parab, M. Asherloo, Q. Guo, L. Chen, A.D. Rollett, Defects and anomalies in powder bed fusion metal additive manufacturing, Current Opinion in Solid State and Materials Science 26(2) (2022) 100974.
- [9] Z. Snow, A.R. Nassar, E.W. Reutzel, Invited Review Article: Review of the formation and impact of flaws in powder bed fusion additive manufacturing, Additive Manufacturing 36 (2020) 101457.
- [10] P.R. Gradl, D.C. Tinker, J. Ivester, S.W. Skinner, T. Teasley, J.L. Bili, Geometric feature reproducibility for laser powder bed fusion (L-PBF) additive manufacturing with Inconel 718, Additive Manufacturing 47 (2021) 102305.
- [11] J.V. Gordon, S.P. Narra, R.W. Cunningham, H. Liu, H. Chen, R.M. Suter, J.L. Beuth, A.D. Rollett, Defect structure process maps for laser powder bed fusion additive manufacturing, Additive Manufacturing 36 (2020) 101552.
- [12] A. Paraschiv, G. Matache, M.R. Condruz, T.F. Frigioescu, L. Pambaguian, Laser Powder Bed Fusion Process Parameters' Optimization for Fabrication of Dense IN 625, Materials, 2022.
- [13] S. Das, D.L. Bourell, S.S. Babu, Metallic materials for 3D printing, MRS Bulletin 41(10) (2016) 729-741.
- [14] M. Seifi, M. Gorelik, J. Waller, N. Hrabe, N. Shamsaei, S. Daniewicz, J.J. Lewandowski, Progress Towards Metal Additive Manufacturing Standardization to Support Qualification and Certification, JOM 69(3) (2017) 439-455.

- [15] Z. Chen, C. Han, M. Gao, S.Y. Kandukuri, K. Zhou, A review on qualification and certification for metal additive manufacturing, Virtual and Physical Prototyping 17(2) (2022) 382-405.
- [16] C.-J. Bae, A.B. Diggs, A. Ramachandran, 6 Quantification and certification of additive manufacturing materials and processes, in: J. Zhang, Y.-G. Jung (Eds.), Additive Manufacturing, Butterworth-Heinemann2018, pp. 181-213.
- [17] A. Thompson, I. Maskery, R.K. Leach, X-ray computed tomography for additive manufacturing: a review, Measurement Science and Technology 27(7) (2016) 072001.
- [18] P.J. Withers, C. Bouman, S. Carmignato, V. Cnudde, D. Grimaldi, C.K. Hagen, E. Maire, M. Manley, A. Du Plessis, S.R. Stock, X-ray computed tomography, Nature Reviews Methods Primers 1(1) (2021) 18.
- [19] A. Du Plessis, S.G. le Roux, J. Waller, P. Sperling, N. Achilles, A. Beerlink, J.-F. Métayer, M. Sinico, G. Probst, W. Dewulf, Laboratory X-ray tomography for metal additive manufacturing: Round robin test, Additive Manufacturing 30 (2019) 100837.
- [20] S. Carmignato, W. Dewulf, R. Leach, Industrial X-ray computed tomography, Springer, Cham, Switzerland, 2018.
- [21] S.C. Jensen, J.D. Carroll, P.R. Pathare, D.J. Saiz, J.W. Pegues, B.L. Boyce, B.H. Jared, M.J. Heiden, Long-term process stability in additive manufacturing, Additive Manufacturing 61 (2023) 103284.
- [22] A.M. Roach, B.C. White, A. Garland, B.H. Jared, J.D. Carroll, B.L. Boyce, Size-dependent stochastic tensile properties in additively manufactured 316L stainless steel, Additive Manufacturing 32 (2020) 101090.
- [23] C. Körner, M. Markl, J.A. Koepf, Modeling and Simulation of Microstructure Evolution for Additive Manufacturing of Metals: A Critical Review, Metallurgical and Materials Transactions A 51(10) (2020) 4970-4983.
- [24] R. Yavari, Z. Smoqi, A. Riensche, B. Bevans, H. Kobir, H. Mendoza, H. Song, K.D. Cole, P. Rao, Part-scale thermal simulation of laser powder bed fusion using graph theory: Effect of thermal history on porosity, microstructure evolution, and recoater crash, Materials & Design 204 (2021) 109685.
- [25] R.J. Williams, A. Piglione, T. Rønneberg, C. Jones, M.-S. Pham, C.M. Davies, P.A. Hooper, In situ thermography for laser powder bed fusion: Effects of layer temperature on porosity, microstructure and mechanical properties, Additive Manufacturing 30 (2019) 100880.
- [26] B. Bevans, C. Barrett, T. Spears, A. Gaikwad, A. Riensche, Z. Smoqi, H. Halliday, P. Rao, Heterogeneous sensor data fusion for multiscale, shape agnostic flaw detection in laser powder bed fusion additive manufacturing, Virtual and Physical Prototyping 18(1) (2023) e2196266.
- [27] A. Riensche, B.D. Bevans, Z. Smoqi, R. Yavari, A. Krishnan, J. Gilligan, N. Piercy, K.D. Cole, P. Rao, Feedforward control of thermal history in laser powder bed fusion: Toward physics-based optimization of processing parameters, Materials & Design 224 (2022) 111351.
- [28] A. Mostafaei, R. Ghiaasiaan, I.T. Ho, S. Strayer, K.-C. Chang, N. Shamsaei, S. Shao, S. Paul, A.-C. Yeh, S. Tin, A.C. To, Additive manufacturing of nickel-based superalloys: A state-of-the-art review on process-structure-defect-property relationship, Progress in Materials Science 136 (2023) 101108.
- [29] H.L. Wei, T. Mukherjee, W. Zhang, J.S. Zuback, G.L. Knapp, A. De, T. DebRoy, Mechanistic models for additive manufacturing of metallic components, Progress in Materials Science (2020) 100703.
- [30] M.M. Francois, A. Sun, W.E. King, N.J. Henson, D. Tourret, C.A. Bronkhorst, N.N. Carlson, C.K. Newman, T. Haut, J. Bakosi, J.W. Gibbs, V. Livescu, S.A. Vander Wiel, A.J. Clarke, M.W. Schraad, T. Blacker, H. Lim, T. Rodgers, S. Owen, F. Abdeljawad, J. Madison, A.T. Anderson, J.L. Fattebert, R.M. Ferencz, N.E. Hodge, S.A. Khairallah, O. Walton, Modeling of additive manufacturing processes for

- metals: Challenges and opportunities, Current Opinion in Solid State and Materials Science 21(4) (2017) 198-206.
- [31] W. King, A. Anderson, R. Ferencz, N. Hodge, C. Kamath, S. Khairallah, Overview of modelling and simulation of metal powder-bed fusion process at Lawrence Livermore National Laboratory, Materials Science and Technology 31(8) (2014) 957-968.
- [32] A. Bandyopadhyay, K.D. Traxel, Invited Review Article: Metal-additive manufacturing—Modeling strategies for application-optimized designs, Additive Manufacturing (2018).
- [33] P. Foteinopoulos, A. Papacharalampopoulos, P. Stavropoulos, On thermal modeling of Additive Manufacturing processes, CIRP Journal of Manufacturing Science and Technology 20 (2018) 66-83.
- [34] Z. Luo, Y. Zhao, A survey of finite element analysis of temperature and thermal stress fields in powder bed fusion Additive Manufacturing, Additive Manufacturing 21 (2018) 318-332.
- [35] M. Grasso, A. Remani, A. Dickins, B.M. Colosimo, R.K. Leach, In-situ measurement and monitoring methods for metal powder bed fusion: an updated review, Measurement Science and Technology 32(11) (2021) 112001.
- [36] S.K. Everton, M. Hirsch, P. Stravroulakis, R.K. Leach, A.T. Clare, Review of in-situ process monitoring and in-situ metrology for metal additive manufacturing, Materials & Design 95 (2016) 431-445.
- [37] T.G. Spears, S.A. Gold, In-process sensing in selective laser melting (SLM) additive manufacturing, Integrating Materials and Manufacturing Innovation 5(1) (2016) 16-40.
- [38] M. Grasso, B.M. Colosimo, Process defects and in situ monitoring methods in metal powder bed fusion: a review, Measurement Science and Technology 28(4) (2017) 044005.
- [39] C. Wang, X.P. Tan, S.B. Tor, C.S. Lim, Machine learning in additive manufacturing: State-of-the-art and perspectives, Additive Manufacturing 36 (2020) 101538.
- [40] Z. Jin, Z. Zhang, K. Demir, G.X. Gu, Machine Learning for Advanced Additive Manufacturing, Matter 3(5) (2020) 1541-1556.
- [41] L. Meng, B. McWilliams, W. Jarosinski, H.-Y. Park, Y.-G. Jung, J. Lee, J. Zhang, Machine Learning in Additive Manufacturing: A Review, JOM 72(6) (2020) 2363-2377.
- [42] D. Mahmoud, M. Magolon, J. Boer, M.A. Elbestawi, M.G. Mohammadi, Applications of Machine Learning in Process Monitoring and Controls of L-PBF Additive Manufacturing: A Review, Applied Sciences 11(24) (2021) 11910.
- [43] A. Gaikwad, B. Giera, G.M. Guss, J.-B. Forien, M.J. Matthews, P. Rao, Heterogeneous sensing and scientific machine learning for quality assurance in laser powder bed fusion A single-track study, Additive Manufacturing 36 (2020) 101659.
- [44] F. Imani, A. Gaikwad, M. Montazeri, P. Rao, H. Yang, E. Reutzel, Process Mapping and In-Process Monitoring of Porosity in Laser Powder Bed Fusion Using Layerwise Optical Imaging, Journal of Manufacturing Science and Engineering 140(10) (2018).
- [45] S. Chowdhury, N. Yadaiah, C. Prakash, S. Ramakrishna, S. Dixit, L.R. Gupta, D. Buddhi, Laser powder bed fusion: a state-of-the-art review of the technology, materials, properties & defects, and numerical modelling, Journal of Materials Research and Technology 20 (2022) 2109-2172.
- [46] Z. Smoqi, A. Gaikwad, B. Bevans, M.H. Kobir, J. Craig, A. Abul-Haj, A. Peralta, P. Rao, Monitoring and prediction of porosity in laser powder bed fusion using physics-informed meltpool signatures and machine learning, Journal of Materials Processing Technology 304 (2022) 117550.

- [47] N.V. Nguyen, A.J.W. Hum, T. Do, T. Tran, Semi-supervised machine learning of optical in-situ monitoring data for anomaly detection in laser powder bed fusion, Virtual and Physical Prototyping 18(1) (2023) e2129396.
- [48] NASA, MSFC-SPEC-3717: Specification for Control and Qualification of Laser Powder Bed Fusion Metallurgical Processes, 2017.
- [49] M.H. Mosallanejad, H. Gashmard, M. Javanbakht, B. Niroumand, A. Saboori, A novel feature engineering approach for predicting melt pool depth during LPBF by machine learning models, Additive Manufacturing Letters 10 (2024) 100214.
- [50] K. Benarji, Y. Ravi Kumar, A.N. Jinoop, C.P. Paul, K.S. Bindra, Effect of Heat-Treatment on the Microstructure, Mechanical Properties and Corrosion Behaviour of SS 316 Structures Built by Laser Directed Energy Deposition Based Additive Manufacturing, Metals and Materials International 27(3) (2021) 488-499.
- [51] N. Jeyaprakash, M. Saravana Kumar, C.-H. Yang, Y. Cheng, N. Radhika, S. Sivasankaran, Effect of microstructural evolution during melt pool formation on nano-mechanical properties in LPBF based SS316L parts, Journal of Alloys and Compounds 972 (2024) 172745.
- [52] T. Zhang, X. Zhou, P. Zhang, Y. Duan, X. Cheng, X. Wang, G. Ding, Hardness Prediction of Laser Powder Bed Fusion Product Based on Melt Pool Radiation Intensity, Materials, 2022.
- [53] A.K. Agrawal, B. Rankouhi, D.J. Thoma, Predictive process mapping for laser powder bed fusion: A review of existing analytical solutions, Current Opinion in Solid State and Materials Science 26(6) (2022) 101024.
- [54] T. Mukherjee, T. DebRoy, A digital twin for rapid qualification of 3D printed metallic components, Applied Materials Today 14 (2019) 59-65.
- [55] Z. Smoqi, L.D. Sotelo, A. Gaikwad, J.A. Turner, P. Rao, Ultrasonic nondestructive evaluation of additively manufactured wear coatings, NDT & E International 133 (2023) 102754.
- [56] Z. Li, X. Zou, F. Bao, F. Gu, A.D. Ball, A Review of Acoustic Emission Monitoring on Additive Manufacturing, in: H. Zhang, G. Feng, H. Wang, F. Gu, J.K. Sinha (Eds.) Proceedings of IncoME-VI and TEPEN 2021, Springer International Publishing, Cham, 2023, pp. 867-878.
- [57] R.J. Smith, M. Hirsch, R. Patel, W. Li, A.T. Clare, S.D. Sharples, Spatially resolved acoustic spectroscopy for selective laser melting, Journal of Materials Processing Technology 236 (2016) 93-102.
- [58] J. Qin, F. Hu, Y. Liu, P. Witherell, C.C.L. Wang, D.W. Rosen, T.W. Simpson, Y. Lu, Q. Tang, Research and application of machine learning for additive manufacturing, Additive Manufacturing 52 (2022) 102691.
- [59] M. Montazeri, A.R. Nassar, A.J. Dunbar, P. Rao, In-process monitoring of porosity in additive manufacturing using optical emission spectroscopy, IISE Transactions 52(5) (2020) 500-515.
- [60] R. Yavari, A. Riensche, E. Tekerek, L. Jacquemetton, H. Halliday, M. Vandever, A. Tenequer, V. Perumal, A. Kontsos, Z. Smoqi, K.D. Cole, P. Rao, Digitally twinned additive manufacturing: Detecting flaws in laser powder bed fusion by combining thermal simulations with in-situ meltpool sensor data, Materials & Design 211 (2021) 110167.
- [61] Z. Yang, Model-based Predictive Analytics for Additive and Smart Manufacturing, Mechanical and Industrial Engineering, University of Massachusetts, Amherst, 2018.
- [62] Z. Yang, D. Eddy, S. Krishnamurty, I. Grosse, P. Denno, Y. Lu, P. Witherell, Investigating Grey-Box Modeling for Predictive Analytics in Smart Manufacturing, ASME, International Design Engineering Technical Conferences and Computers and Information in Engineering Conference, Cleaveland, OH, 2017, pp. V02BT03A024-034.

- [63] M. Ghayoomi Mohammadi, D. Mahmoud, M. Elbestawi, On the application of machine learning for defect detection in L-PBF additive manufacturing, Optics & Laser Technology 143 (2021) 107338.
- [64] O. Zinovieva, A. Zinoviev, V. Ploshikhin, Three-dimensional modeling of the microstructure evolution during metal additive manufacturing, Computational Materials Science 141 (2018) 207-220.
- [65] J.H.K. Tan, S.L. Sing, W.Y. Yeong, Microstructure modelling for metallic additive manufacturing: a review, Virtual and Physical Prototyping 15(1) (2020) 87-105.
- [66] T. Gatsos, K.A. Elsayed, Y. Zhai, D.A. Lados, Review on Computational Modeling of Process–Microstructure–Property Relationships in Metal Additive Manufacturing, JOM 72(1) (2020) 403-419.
- [67] R. Acharya, J.A. Sharon, A. Staroselsky, Prediction of microstructure in laser powder bed fusion process, Acta Materialia 124 (2017) 360-371.
- [68] J.G. Pauza, W.A. Tayon, A.D. Rollett, Computer simulation of microstructure development in powder-bed additive manufacturing with crystallographic texture, Modelling and Simulation in Materials Science and Engineering 29(5) (2021) 055019.
- [69] M. Markl, C. Körner, Multiscale Modeling of Powder Bed–Based Additive Manufacturing, Annual Review of Materials Research 46(Volume 46, 2016) (2016) 93-123.
- [70] J.A. Turner, J. Belak, N. Barton, M. Bement, N. Carlson, R. Carson, S. DeWitt, J.-L. Fattebert, N. Hodge, Z. Jibben, W. King, L. Levine, C. Newman, A. Plotkowski, B. Radhakrishnan, S.T. Reeve, M. Rolchigo, A. Sabau, S. Slattery, B. Stump, ExaAM: Metal additive manufacturing simulation at the fidelity of the microstructure, The International Journal of High Performance Computing Applications 36(1) (2022) 13-39.
- [71] T.W. Heo, S.A. Khairallah, R. Shi, J. Berry, A. Perron, N.P. Calta, A.A. Martin, N.R. Barton, J. Roehling, T. Roehling, A mesoscopic digital twin that bridges length and time scales for control of additively manufactured metal microstructures, Journal of Physics: Materials 4(3) (2021) 034012.
- [72] M. Liu, S. Fang, H. Dong, C. Xu, Review of digital twin about concepts, technologies, and industrial applications, Journal of Manufacturing Systems 58 (2021) 346-361.
- [73] A. Gaikwad, R. Yavari, M. Montazeri, K.D. Cole, L. Bian, P. Rao, Toward the digital twin of additive manufacturing: Integrating thermal simulations, sensing, and analytics to detect process faults, IISE Transactions 52(11) (2020) 1204-1217.
- [74] N. Kouraytem, X. Li, W. Tan, B. Kappes, A.D. Spear, Modeling process–structure–property relationships in metal additive manufacturing: a review on physics-driven versus data-driven approaches, Journal of Physics: Materials 4(3) (2021) 032002.
- [75] T. Shen, B. Li, Digital twins in additive manufacturing: a state-of-the-art review, The International Journal of Advanced Manufacturing Technology 131(1) (2024) 63-92.
- [76] D.R. Gunasegaram, A.B. Murphy, A. Barnard, T. DebRoy, M.J. Matthews, L. Ladani, D. Gu, Towards developing multiscale-multiphysics models and their surrogates for digital twins of metal additive manufacturing, Additive Manufacturing 46 (2021) 102089.
- [77] L. Zhang, X. Chen, W. Zhou, T. Cheng, L. Chen, Z. Guo, B. Han, L. Lu, Digital Twins for Additive Manufacturing: A State-of-the-Art Review, Applied Sciences, 2020.
- [78] S. Guo, M. Agarwal, C. Cooper, Q. Tian, R.X. Gao, W. Guo, Y.B. Guo, Machine learning for metal additive manufacturing: Towards a physics-informed data-driven paradigm, Journal of Manufacturing Systems 62 (2022) 145-163.
- [79] S.C. Feng, A.T. Jones, G. Shao, Data Requirements for Digital Twins in Additive Manufacturing, ASME 2023 18th International Manufacturing Science and Engineering Conference, 2023.

- [80] R.B. Roy, D. Mishra, S.K. Pal, T. Chakravarty, S. Panda, M.G. Chandra, A. Pal, P. Misra, D. Chakravarty, S. Misra, Digital twin: current scenario and a case study on a manufacturing process, The International Journal of Advanced Manufacturing Technology 107(9) (2020) 3691-3714.
- [81] A.R. Riensche, B.D. Bevans, G. King, A. Krishnan, K.D. Cole, P. Rao, Predicting meltpool depth and primary dendritic arm spacing in laser powder bed fusion additive manufacturing using physics-based machine learning, Materials & Design 237 (2024) 112540.
- [82] G. Mohr, S.J. Altenburg, A. Ulbricht, P. Heinrich, D. Baum, C. Maierhofer, K. Hilgenberg, In-Situ Defect Detection in Laser Powder Bed Fusion by Using Thermography and Optical Tomography—Comparison to Computed Tomography, Metals, 2020.
- [83] V. Manvatkar, A. De, T. DebRoy, Spatial variation of melt pool geometry, peak temperature and solidification parameters during laser assisted additive manufacturing process, Materials Science and Technology 31(8) (2015) 924-930.
- [84] K. Taherkhani, O. Ero, F. Liravi, S. Toorandaz, E. Toyserkani, On the application of in-situ monitoring systems and machine learning algorithms for developing quality assurance platforms in laser powder bed fusion: A review, Journal of Manufacturing Processes 99 (2023) 848-897.
- [85] J. Munk, E. Breitbarth, T. Siemer, N. Pirch, C. Häfner, Geometry Effect on Microstructure and Mechanical Properties in Laser Powder Bed Fusion of Ti-6Al-4V, Metals, 2022.
- [86] W.M. Tucho, V. Hansen, Characterization of SLM-fabricated Inconel 718 after solid solution and precipitation hardening heat treatments, Journal of Materials Science 54(1) (2019) 823-839.
- [87] J.P. Oliveira, T.G. Santos, R.M. Miranda, Revisiting fundamental welding concepts to improve additive manufacturing: From theory to practice, Progress in Materials Science 107 (2020) 100590.
- [88] M. Gouge, P. Michaleris, Thermo-mechanical modeling of additive manufacturing, Butterworth-Heinemann2017.
- [89] D. Sarkar, A. Kapil, A. Sharma, Advances in computational modeling for laser powder bed fusion additive manufacturing: A comprehensive review of finite element techniques and strategies, Additive Manufacturing 85 (2024) 104157.
- [90] B. Schoinochoritis, D. Chantzis, K. Salonitis, Simulation of metallic powder bed additive manufacturing processes with the finite element method: A critical review, Proceedings of the Institution of Mechanical Engineers, Part B: Journal of Engineering Manufacture 231(1) (2015) 96-117.
- [91] J. Baiges, M. Chiumenti, C.A. Moreira, M. Cervera, R. Codina, An adaptive Finite Element strategy for the numerical simulation of additive manufacturing processes, Additive Manufacturing 37 (2021) 101650.
- [92] R. Yavari, R. Williams, A. Riensche, P.A. Hooper, K.D. Cole, L. Jacquemetton, H. Halliday, P.K. Rao, Thermal modeling in metal additive manufacturing using graph theory Application to laser powder bed fusion of a large volume impeller, Additive Manufacturing 41 (2021) 101956.
- [93] K.D. Cole, A. Riensche, P.K. Rao, Discrete Green's functions and spectral graph theory for computationally efficient thermal modeling, International Journal of Heat and Mass Transfer 183 (2022) 122112.
- [94] K.D. Cole, M.R. Yavari, P.K. Rao, Computational heat transfer with spectral graph theory: Quantitative verification, International Journal of Thermal Sciences 153 (2020) 106383.
- [95] J. Ye, S.A. Khairallah, A.M. Rubenchik, M.F. Crumb, G. Guss, J. Belak, M.J. Matthews, Energy Coupling Mechanisms and Scaling Behavior Associated with Laser Powder Bed Fusion Additive Manufacturing, Advanced Engineering Materials 21(7) (2019) 1900185.

- [96] W.H. Kan, Y. Nadot, M. Foley, L. Ridosz, G. Proust, J.M. Cairney, Factors that affect the properties of additively-manufactured AlSi10Mg: Porosity versus microstructure, Additive Manufacturing 29 (2019) 100805.
- [97] A. Pandey, A. Jain, Comparative analysis of KNN algorithm using various normalization techniques, International Journal of Computer Network and Information Security 11(11) (2017) 36.
- [98] P. Dangeti, Statistics for machine learning, Packt Publishing Ltd2017.
- [99] A. Shrivastava, S. Anand Kumar, S. Rao, B.K. Nagesha, Exploring How LPBF process parameters impact the interface characteristics of LPBF Inconel 718 deposited on Inconel 718 wrought substrates, Optics & Laser Technology 174 (2024) 110571.
- [100] S. Kurian, R. Mirzaeifar, Deformation mechanisms of the subgranular cellular structures in selective laser melted 316L stainless steel, Mechanics of Materials 148 (2020) 103478.
- [101] W. Liu, N. Yan, H. Wang, Dendritic morphology evolution and microhardness enhancement of rapidly solidified Ni-based superalloys, Science China Technological Sciences 62(11) (2019) 1976-1986.
- [102] X. Wang, J. Wang, J. Kang, T. Wang, P. Wu, T. Feng, L. Zheng, Y. Rong, High-throughput investigation of laser powder bed fabricated Inconel 718 alloy: Fabrication, microstructure and performance, Materials Today Communications 27 (2021) 102303.

## Acknowledgments

Prahalada Rao acknowledges funding from the National Science Foundation (NSF) via grant numbers: CMMI-2309483/1752069, OIA-1929172, PFI-TT 2322322/2044710, CMMI-1920245, ECCS-2020246, CMMI-1739696, and CMMI-1719388; Department of the Navy, Office of Naval Research (ONR, N00014-21-1-2781) and Naval Surface Warfare Center (NAVAIR, N6833524C0215); and the National Institute of Standards and Technology (NIST) via grant 70NANB23H029T for supporting his research program.

- Understanding the causal influence of process parameters and thermal history on part quality using insitu sensing was the major aspect of CMMI-2309483/1752069 (Program Officer: Andrew Wells).
- Commercialization of the graph theory thermal approach for ultrafast simulation of metal additive manufacturing processes is being pursued under PFI-TT 2322322/2044710 (Program Officer: Samir Iqbal).
- Predicting (detecting) flaws in laser powder bed fusion by combining thermal simulations with in-situ sensor data was funded via NIST 70NANB23H029T.

This work was made possible by the use of Virginia Tech's Materials Characterization Facility, which is supported by the Institute for Critical Technology and Applied Science, the Macromolecules Innovation Institute, and the Office of the Vice President for Research and Innovation